MJO Moisture Budget during DYNAMO in a Cloud-Resolving Model

Matthew A. Janiga and Chidong Zhang

Rosenstiel School of Marine and Atmospheric Science, University of Miami, Miami, Florida

ABSTRACT

Contributions by different physical processes and cloud types to the sum of the large-scale vertical moisture advection and apparent moisture sink observed by the DYNAMO field campaign northern sounding array during the passage of a Madden–Julian oscillation (MJO) event are estimated using a cloud-resolving model. The sum of these two moisture budget terms is referred to as the column-confined moisture tendency M_C. Assuming diabatic balance, the contribution of different physical processes and cloud types to the large-scale vertical velocity and M_C can be estimated using simulated diabatic tendencies and the domain-averaged static stability and vertical moisture gradient. Low-level moistening preceding MJO passage is captured by M_C and dominated by the effects of shallow clouds. Because of the large vertical moisture gradient at this level, condensational heating in these clouds generates ascent and vertical moisture advection overwhelming the removal of water vapor by condensation. Shallow convective eddy transport also contributes to low-level moistening during this period. Eddy transport by congestus and deep convective clouds contributes to subsequent mid- and upper-level moistening, respectively, as well as low-level drying. Because the upper-level vertical moisture gradient is small, ice deposition within stratiform clouds has a net drying effect. The weak eddy transport in stratiform clouds is unable to compensate for this drying. Nonprecipitating clouds mainly modulate M_C through their effects on radiation. During the enhanced phase, reduced longwave cooling results in less subsidence and drying; the opposite occurs during the suppressed phase. Large-scale horizontal advection, which is not included in M_C, is responsible for much of the drying during the dissipating phase.

1. Introduction

The Madden–Julian oscillation (MJO) is a planetary-scale phenomenon that modulates convective activity in the tropics on intraseasonal time scales (30–100 days) (Madden and Julian 1971, 1972). The MJO is characterized by an envelope of increased rainfall and free-tropospheric water vapor that originates over the Indian Ocean, propagates eastward at 5–8 m s^{-1}, and dissipates over the central Pacific. This convective envelope modulates rainfall and tropical cyclogenesis as it propagates while the associated latent heat release generates teleconnection patterns that affect global weather and climate (e.g., Zhang 2005, 2013). The ability of global operational and climate models to capture moisture–convection interactions within this convective envelope is closely related to their being able to simulate its growth and propagation (e.g., Bechtold et al. 2008;

Hirons et al. 2013b,a; Kim et al. 2014; Klingaman et al. 2015).

Observational studies have demonstrated that, moving eastward across the convective envelope, the dominant cloud type transitions from shallow convection to congestus, to deep convection, to stratiform (Deng et al. 2013). The coincidence of low-level moistening and both shallow and congestus clouds ahead of the MJO envelope has led many studies to infer that these cloud types contribute significantly to this moistening (e.g., Johnson et al. 1999; Benedict and Randall 2007). At long time scales and large spatial scales in the tropics, vertical velocity is closely related to the diabatic heating within clouds (Sobel et al. 2001). Taking advantage of this fact, Chikira (2014) used a global model with parameterized convection to examine the contribution of different physics processes to the moisture tendency observed during the passage of an MJO envelope. This included the contribution of each process to the large-scale moisture advection diagnosed by relating large-scale velocity and simulated diabatic heating. In this study, we take a similar approach but instead use a cloud-resolving

---

Corresponding author address: Matthew A. Janiga, Naval Research Laboratory, 7 Grace Hopper Ave., Monterey, CA 93943.
E-mail: matthew.janiga.ctr@nrlmry.navy.mil

model (CRM) to examine the contribution of individual physics processes and cloud types to the evolution of moisture.

"Moisture mode" theories of the MJO (Raymond 2001; Raymond and Fuchs 2009; Sobel and Maloney 2012, 2013; Adames and Kim 2016) hypothesize that the growth/dissipation and movement of moisture anomalies is critical to the development and characteristics of the eastward-moving convective envelope observed in the Indian Ocean and west Pacific associated with the MJO. This is supported by modeling experiments, which have shown that simulating MJO-like convective envelopes requires the cumulus parameterization to be sensitive to moisture (Maloney 2009; Hannah and Maloney 2011, 2014) and that this feature cannot develop when the growth of moisture anomalies is suppressed (Grabowski and Moncrieff 2004).

On the scale of the MJO, column-integrated moist static energy (MSE) anomalies, which are equivalent to column water vapor anomalies under the weak temperature gradient (WTG) approximation, amplify through increased surface fluxes (Sobel et al. 2010) and reduced radiative cooling (Ma and Kuang 2011). The modulation of horizontal advection by synoptic-scale eddies on the eastern side of the MJO envelope (Maloney 2009; Kiranmayi and Maloney 2011; Andersen and Kuang 2012) and the intense dry air advection by westerlies on the western side of the MJO envelope (Kerns and Chen 2014) appear to play an important role in explaining the eastward movement of the MJO. Vertical advection may also contribute to the eastward propagation of the MJO through shallow and congestus moistening on the leading edge of the convective envelope but likely cannot explain why eastward propagation is selected over westward propagation (Masunaga and L'Ecuyer 2014; Sobel et al. 2014; Wang et al. 2015).

The Dynamics of the MJO (DYNAMO)/ARM MJO Investigation Experiment (AMIE)/Cooperative Indian Ocean Experiment on Intraseasonal Variability (CINDY) field campaign (herein referred to as DYNAMO) collected an unprecedented quantity of observations in the Indian Ocean from October 2011 to March 2012 (Yoneyama et al. 2013; Zhang 2013). The properties and behavior of convection during DYNAMO were well observed by numerous radars operating at a variety of wavelengths (Powell and Houze 2013; Zuluaga and Houze 2013; Deng et al. 2014). In addition, the apparent heat source Q_1 and moisture sink Q_2 (Yanai et al. 1973), as well as the large-scale advective tendencies, were derived using observations from two sounding arrays (Johnson and Ciesielski 2013; Ciesielski et al. 2014; Johnson et al. 2015).

Assuming that they reproduce the frequency and properties of different cloud types, CRMs forced by large-scale advective tendencies can be used to estimate the contributions of these cloud types to Q_1 and Q_2 (e.g., Tao et al. 2003). However, Q_2 is only one part of the moisture budget. In tropical regions with high rain rates, there is often a large cancellation between the drying due to Q_2 and the large-scale vertical moisture advection (Chikira 2014). In such regimes, the vertical velocity can be related to Q_1 by assuming that vertical potential temperature advection and Q_1 are balanced. This is closely related to the WTG and weak pressure gradient or damped-wave approximations, which have been applied interactively within several CRM studies in what is known as parameterized large-scale dynamics (Mapes 2004; Kuang 2008; Wang and Sobel 2011, 2012; Wang et al. 2013).

Chikira (2014) examined the contribution of individual physics processes to the sum of Q_2 and the vertical moisture advection. We refer to this term as the column-confined moisture tendency M_C, since it accounts for all processes within a column but not the exchanges between columns associated with horizontal advection. The vertical moisture advection in M_C can be taken directly from the sounding observations or approximated using the vertical velocity calculated by assuming a balance between diabatic heating and vertical potential temperature advection and the vertical moisture gradient. However, the column under consideration must cover a large spatial scale for the approximation of diabatic balance to hold. The vertical velocity calculated by assuming diabatic balance can also be decomposed into its component parts using the contributions of various physical processes to diabatic heating.

Making use of these assumptions and relationships, Chikira (2014) showed that the reduced radiative cooling within the convective envelope of the MJO is associated with anomalous moistening by the large-scale vertical moisture advection. Furthermore, although the proximate effect of condensation from the cumulus parameterization was to dry much of the free troposphere, the heating produced by the condensation is associated with large-scale vertical moisture advection, which overwhelms this drying at low levels. This is because the low-level vertical moisture gradient is large. In contrast, the ultimate effect of condensation was to dry the upper levels, since the vertical moisture gradient is small at that level. Chikira (2014) also found that the cooling associated with melting snow induced midlevel subsidence and drying, while high-frequency (<20 day) variations in vertical moisture advection moistened the upper levels.

In this study, a CRM forced by the advective tendencies derived for the northern sounding array (NSA)

is used to simulate one of the MJO events during DYNAMO. Output from the simulation is used to diagnose the contribution of different physics processes (microphysics, eddy transport, and radiation) and individual cloud types to the evolution of moisture, accounting for both their direct effect on moisture and their indirect effect on large-scale vertical moisture advection diagnosed using simulated diabatic heating and the assumption of diabatic balance.

The numerical model, physics parameterizations, and simulation setup are described in section 2. In section 3, the results of the simulation are described. This begins with an overview of the moisture variability during the simulation and analyses of simulated diabatic tendencies. This is followed by an analysis of the validity of the diabatic balance framework used for diagnosing the moisture budget and concludes with an examination of the roles that different physical processes and cloud types play in the time evolution of moisture. Section 4 summarizes the results and discusses their broader implications and relationship with previous studies.

2. Model description and methodology

a. Model description

The model used in this study is the System for Atmospheric Modeling (SAM), version 6.8.2 (Khairoutdinov and Randall 2003). The model solves the equations of motion using the anelastic approximation. Microphysics are parameterized using the two-moment Morrison scheme, which has five prognostic hydrometeor types (cloud water q_c, cloud ice q_i, rain q_r, snow q_s, and graupel q_g) (Morrison et al. 2005, 2009). Radiation processes are parameterized using the Rapid Radiative Transfer Model (RRTM) scheme (Iacono et al. 2008), and subgrid turbulence is parameterized using the Smagorinsky scheme.

The prognostic thermodynamic variable, liquid–ice static energy ($s_{li} = C_p T + gz - L_c q_{liq} - L_s q_{ice}$), is conserved for advection and phase changes but not hydrometeor sedimentation. Here, C_p is the specific heat of dry air at constant pressure, T is the temperature, g is gravity, z is the height, L_c and L_s are the latent heat of evaporation and sublimation, and q_{liq} and q_{ice} are the liquid and frozen hydrometeor mixing ratios.

The cloud water mixing ratio is computed using saturation adjustment and advected in combination with the water vapor mixing ratio q_v. The cloud water mixing ratio is also advected by itself as a tracer variable so that q_v can be diagnosed. The potential temperature and water vapor mixing ratio tendency associated with

advection, diffusion, and microphysics is determined from the difference in these quantities before and after specific physics process are computed.

b. Data and simulation setup

The simulation in this study uses a commonly employed framework in which observed large-scale advective tendencies of potential temperature and water vapor mixing ratio are used to drive the evolution of clouds in a CRM with periodic boundary conditions. The simulation was performed using 3-hourly data from the DYNAMO northern sounding array, since this array captured more convective variability on the MJO time scale (Johnson and Ciesielski 2013). Version 2a of the sounding data, which is based only on observations, was used. The goal of the simulation is not to determine the total value of Q_1 and Q_2, since these are constrained by the forcing, but the contributions of different physical processes and cloud types to Q_1 and Q_2. The total large-scale advective tendencies of potential temperature θ and water vapor q_v are

$$Q_{\text{TLSA}} = -\overline{\mathbf{v}} \cdot \nabla \overline{\theta} - \overline{w} \frac{\partial \overline{\theta}}{\partial z} \quad \text{and} \quad (1)$$

$$M_{\text{TLSA}} = -\overline{\mathbf{v}} \cdot \nabla \overline{q}_v - \overline{w} \frac{\partial \overline{q}_v}{\partial z}. \quad (2)$$

Here, $\overline{\mathbf{v}}$ is the vector wind and w is the vertical velocity. Overbars denote horizontal averages over the array. As in Varble et al. (2011) and Fridlind et al. (2012), model horizontal winds are nudged to observations at a 2-h time scale, which is sufficient to allow for the development of mesoscale circulations (Xu and Randall 1996). To prevent model drift due to errors in the sounding array budget and model physics, domain-averaged potential temperature and water vapor in the simulation are nudged to NSA average profiles at a 6-h time scale. In previous CRM studies, this has been shown to improve the overall properties of simulated clouds (Varble et al. 2011; Fridlind et al. 2012). Simulations that exclude temperature and water vapor nudging are able to produce a sustained period of enhanced moisture during the passage of the MJO but have moisture biases that lead to a poorer representation of the transition from shallow to deep convection observed by radar. In addition, daily sea surface temperatures (SST) from the Objectively Analyzed Air–Sea Fluxes (OAFlux) product (Yu and Weller 2007) are used as boundary conditions in the simulation instead of prescribing the surface sensible and latent heat fluxes.

The version 7 TRMM 3B42 rain product (Huffman et al. 2007) and sounding- and radar-derived rain rates
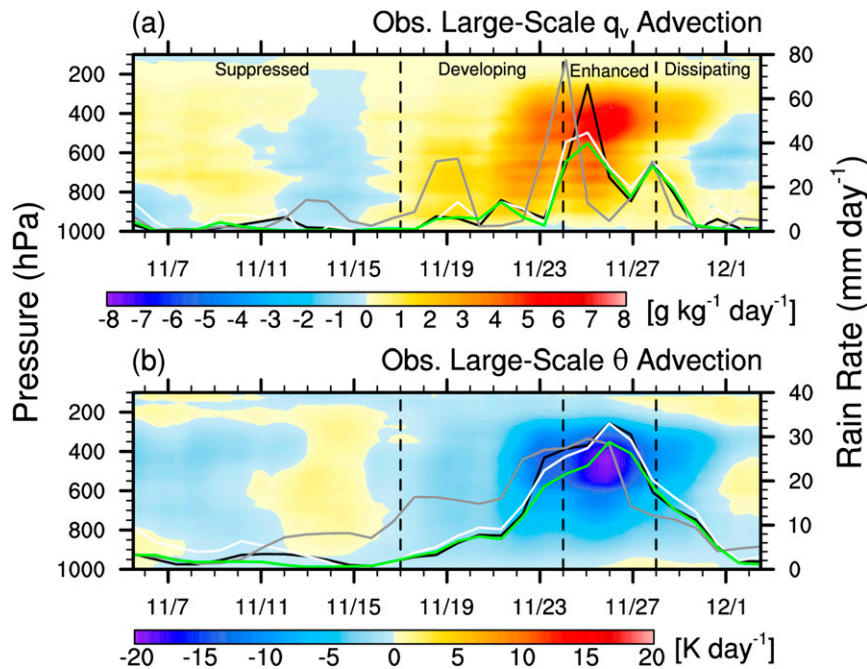
FIG. 1. The 5-day boxcar-averaged large-scale total advection of (a) water vapor $(g\,kg^{-1}\,day^{-1})$ and (b) potential temperature $(K\,day^{-1})$ and (a) daily and (b) 5-day boxcar-averaged 3B42 (black), Q_2-derived (white), 1-km S-Pol (gray), and surface simulated (green) rain rate $(mm\,day^{-1})$. In all subsequent plots, 5-day boxcar averaging is also applied to shaded fields and rain time series. The MJO event is separated into four phases: suppressed (1–17 Nov), developing (17–24 Nov), enhanced (24–28 Nov), and dissipating (28 Nov–5 Dec).

are compared to the simulation. Sounding-derived rain rates are calculated using the observed Q_2. Observed reflectivity and rain rates are from the S-band dual-Doppler polarimeteric radar (S-Pol) survey scans (Powell and Houze 2013). These were gridded to a 2-km horizontal and 500-m vertical resolution Cartesian grid.

The simulation covers the period 1 November–5 December; the first 48 h are excluded to account for model spinup. The model domain is $256 \times 256\,km^2$ in the horizontal with 1-km grid spacing and a stretched vertical grid with 106 levels extending from the surface to 30 km with a 250-m grid spacing in the free troposphere. The size of this horizontal domain is larger than that used in previous periodic CRM simulations that were able to develop robust mesoscale circulations (Varble et al. 2011). Damping is applied to the upper 10 km. The horizontal grid spacing is fairly coarse for resolving deep convective cloud-scale circulations (e.g., Bryan et al. 2003) and especially coarse for resolving the circulations within shallow clouds (e.g., Brown 1999; Cheng and Xu 2008; Cheng et al. 2010; Matheou et al. 2011). However, this compromise is necessary to simulate the passage of the MJO convective envelope on a periodic computational domain large enough to permit the development of mesoscale circulations. Sensitivity tests with

horizontal grid spacings of 125–4000 m and vertical grid spacings of up to 125 m were performed during the transition from shallow to deep convection. Deep convection is relatively insensitive to resolution, congestus rain rates decrease by half when horizontal grid spacing is decreased to 4000 m, stratiform rain rates increase as resolution is decreased, and shallow nonprecipitating clouds are more frequent at higher resolutions. While the partitioning of rain rate Q_1 and Q_2 between cloud types is sensitive to model resolution, the total values are not.

The evolution of the observed large-scale advective tendencies used to force the simulation is shown in Fig. 1. Similar to Sobel et al. (2014), most time–height plots and rain rates in this study have been smoothed with a 5-day moving average to highlight intraseasonal time-scale processes. However, daily observed and simulated rain rates are shown in Fig. 1a to show that the MJO time scale envelope of enhanced rain rates is modulated by higher-frequency events. Large-scale moistening and cooling, displaying a transition from bottom- to top-heavy profiles, are observed during the convectively enhanced phase, while small amounts of drying and heating occur during the most suppressed conditions. Because of the constraint of prescribed

thermodynamic forcing, rainfall from the simulation and sounding array are in close agreement. The S-Pol radar is located near the southwest corner of the NSA and therefore tends to lead the rainfall over the sounding array. The 3-hourly large-scale moisture advection is highly variable in time and the vertical—even compared to the 3-hourly potential temperature advection. When a 5-day moving average is applied to this field, horizontal stripes appear (Fig. 1a). These horizontal stripes are a result of the temporal averaging; they do not occur at preferred levels and are not apparent in the 3-hourly data (P. E. Ciesielski 2016, personal communication).

c. Cloud type identification

Cloud types are identified using both observed S-Pol and simulated reflectivity. Similar to Varble et al. (2011), simulated Rayleigh regime radar reflectivity is calculated by integrating the sixth moment of the rain, snow, and graupel mixing ratios, taking into account the number concentrations and assumed size distributions in the Morrison microphysics scheme. Dielectric factors in the radar calculation follow Smith (1984).

The first step in identifying the cloud types is applying the algorithm of Steiner et al. (1995) to the 1-km-altitude S-Pol and surface simulated reflectivity. Because low-level stratiform echoes rarely exceed 40 dBZ (e.g., Penide et al. 2013), grid points with reflectivity exceeding this value are designated convective cells; the same criteria are applied to DYNAMO radar data in Deng et al. (2014) and Xu and Rutledge (2014). Grid points with high reflectivity peakedness or roughness are also identified as convective cells; this follows Eq. (B1) of Yuter and Houze (1997), where the radius used to calculate the background reflectivity is 11 km, and the tunable parameters a and b are 16 and 64, respectively. Convective cells are then radially expanded based on the background reflectivity using the parameters in Fig. 6b of Steiner et al. (1995).

To ensure reliable detection by S-Pol, precipitating cloud types (shallow convection, congestus, deep convection, and stratiform) detected in the S-Pol and simulated reflectivity are required to have a reflectivity exceeding 0 dBZ at 1 km and the surface, respectively. All grid points with >0 dBZ low-level echoes and 0 dBZ echo tops <4 km are identified as shallow convection. Of these grid points, most of the rainfall comes from grid points identified as convective based on their low-level reflectivity texture; the few identified as stratiform based on their low-level reflectivity texture have heating and moistening profiles consistent with shallow convection. Congestus and deep convective clouds are identified by a convective

low-level reflectivity texture and 0-dBZ echo tops between 4 and 7 km and greater than 7 km, respectively. The echo top criteria used to distinguish congestus clouds from shallow and deep convective clouds is similar to that in Wall et al. (2013) and Schumacher et al. (2015). Hydrometeor profiles of the simulated shallow convective clouds indicate they are entirely driven by warm-rain processes. In contrast, the simulated congestus clouds are weakly glaciated, consistent with Johnson et al. (1999) and Wall et al. (2013); however, they have dramatically less graupel than the deep convective clouds (Rowe and Houze 2014). Stratiform clouds are identified by a stratiform low-level reflectivity texture and echo tops >4 km. This ensures that stratiform clouds have depositional ice growth aloft and low-level evaporation, resulting in heating and moistening profiles that are consistent with observations (e.g., Yang and Smith 2000). Grid points that do not fall into the above categories are designated weakly and nonprecipitating clouds and contain the weakest shallow convective clouds, anvil, and clear sky.

3. Results

a. Evolution of moisture and diabatic processes

Figure 2 shows the time evolution of observed and simulated moisture anomalies. Both the observed and domain-averaged simulated moisture anomalies are calculated with respect to the mean observed q_v profile during 3 November–5 December. Because of the application of thermodynamic nudging, the observed and simulated moisture evolutions are in close agreement.

The average simulated rain rate is considerably lower than the average S-Pol rain rate but closer to the sounding-derived and TRMM 3B42 rain rate (Table 1). The average simulated shallow convective rain rate is over twice that in S-Pol, even though the cloud type covers less area in the simulation. At horizontal grid spacings of 125 and 250 m, the shallow convective rain rate more closely matches observations. The average congestus rain rate and area are lower in the simulation than in S-Pol (Table 1). Average simulated and radar-observed deep convective rain rates are similar, but the deep convective area is greater in the simulation. In contrast, the average stratiform rain rate in S-Pol greatly exceeds the simulated value even though the simulated stratiform area is greater. Comparing the distributions of simulated and S-Pol stratiform rain rates shows that the simulation significantly underestimates the frequency of 1–10 mm h^{-1} rain rates (not shown); this occurs in most bulk microphysical schemes (Varble et al. 2011).
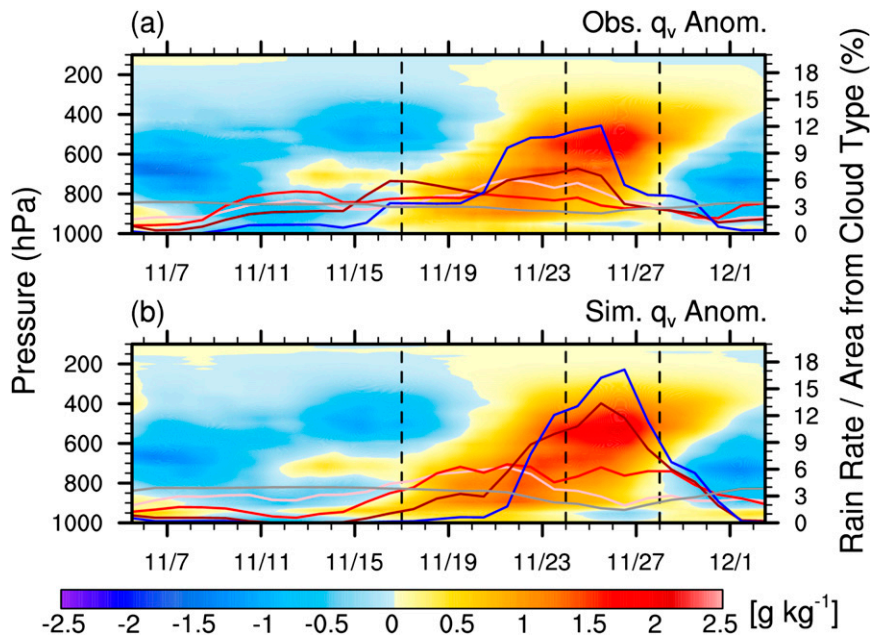
FIG. 2. (a) Observed and (b) simulated water vapor mixing ratio anomalies (g kg^{-1}) (anomalies are with respect to the observed 3 Nov–5 Dec mean) and the fraction of the cumulative rain rate (area) from precipitating cloud types (weakly and nonprecipitating cloud) from (a) S-Pol and (b) the simulation. Lines indicate the shallow convective (pink), congestus (red), deep convective (dark red), stratiform (blue), and weakly/nonprecipitating (gray) cloud types.

Figure 2 also shows the fraction of the rain rate (or rain area in the case of weakly and nonprecipitating cloud) from S-Pol and the simulation at each time. Compared to S-Pol, the simulation underestimates (overestimates) the fraction of deep convective and stratiform rain, which occurs during the dry (wet) periods.

The apparent heat source Q_1 and moisture sink Q_2 (Yanai et al. 1973) at each grid point can be expressed as follows:

$$Q_1 \equiv \overline{\pi}\left(\frac{\partial\overline{\theta}}{\partial t} + \overline{\mathbf{V}}\cdot\nabla\overline{\theta} + \overline{w}\frac{\partial\overline{\theta}}{\partial z}\right)$$

$$= \overline{\pi}\left(-\frac{1}{\overline{\rho}}\frac{\partial\overline{\rho}\overline{w'\theta'}}{\partial z} - \nabla\cdot\overline{\mathbf{V}'\theta'} + Q_D\right)$$

$$+ Q_M + Q_R + \overline{Q}_N \quad \text{and} \tag{3}$$

$$Q_2 \equiv -\frac{L_v}{C_p}\left(\frac{\partial\overline{q}_v}{\partial t} + \overline{\mathbf{V}}\cdot\nabla\overline{q}_v + \overline{w}\frac{\partial\overline{q}_v}{\partial z}\right)$$

$$= \frac{L_v}{C_p}\left(-\frac{1}{\overline{\rho}}\frac{\partial\overline{\rho}\overline{w'q_v'}}{\partial z} - \nabla\cdot\overline{\mathbf{V}'q_v'} + M_D + M_M + \overline{M}_N\right), \tag{4}$$

where Q_D, Q_M, and Q_R are the tendency of potential temperature θ due to diffusion, microphysics, and radiation; M_D and M_M are the q_v tendency due to diffusion and microphysics; L_v is the latent heat of vaporization; $\overline{\pi} = (p/P_0)^{R/C_p}$ is the Exner function, where $P_0 = 1000$ hPa is the reference pressure; and R is the gas constant for dry air. Overbars indicate horizontal averages, and primes indicate deviations from the horizontal averages. As in Tao et al. (2003),

TABLE 1. Simulated surface and S-Pol 1-km mean rain rates (mm day^{-1}) and area coverage (%) during 3 Nov–5 Dec for each cloud type. The mean rain rates for the Q_2-based sounding estimate and TRMM 3B42 product are 9.36 and 8.20 mm day^{-1}, respectively.

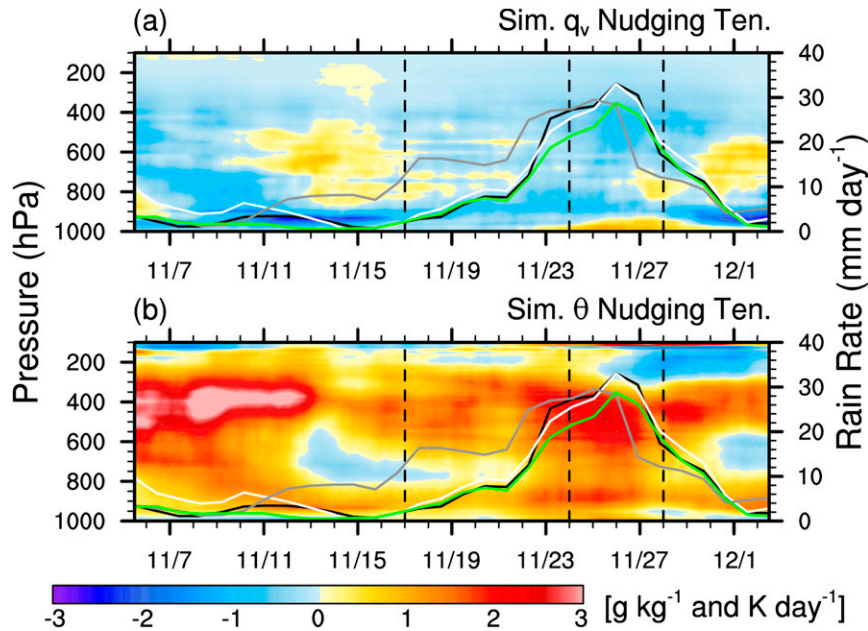| Cloud type	Simulated rain rate	S-Pol rain rate	Simulation area	S-Pol area
Total	7.16	11.19	—	—
Shallow convective	0.41	0.16	2.67	3.37
Congestus	0.71	1.77	0.49	1.10
Deep convective	4.93	5.14	2.08	1.26
Stratiform	1.12	4.10	12.09	9.38
Weakly and nonprecipitating	0.02	0.01	82.68	84.88

FIG. 3. Simulated (a) water vapor (g kg^{-1} day^{-1}) and (b) potential temperature (K day^{-1}) nudging tendency. Rain-rate convention follows Fig. 1b.

overbars are excluded from the eddy terms since Q_1 and Q_2 are evaluated at individual grid points and for specific cloud types.

The terms Q_N and M_N are the θ and q_v tendencies due to thermodynamic nudging; the overbars indicate that they are uniformly applied across the domain. These terms represent the heat and moisture tendencies necessary to compensate for errors in the sounding array budget and model physics. Because they are applied uniformly across the domain, they cannot be decomposed by cloud type.

Since the main interest of this study is the moisture budget, we focus on the quantity $-Q_2 C_p/L_v$. When considering averages of Q_1 and $-Q_2 C_p/L_v$ over the entire domain, the potential temperature and moisture tendencies due to advection (Q_A and M_A), calculated as the difference in these fields before and after calling advection, are used in place of the eddy flux convergence terms. This produces a slightly poorer budget closure.

Figure 3 shows the simulated water vapor and potential temperature nudging tendencies. The persistent drying and heating by the nudging tendency at 900 hPa may be because of biases in the simulated shallow convection due to the coarse resolution of the simulation (e.g., Cheng et al. 2010). It could also be due to excessive low-level rainwater evaporation by precipitating cloud systems (Bryan and Morrison 2012). Throughout the simulation—but especially from 3 to 13 November—nudging potential

temperature to observed values results in heating between 300 and 600 hPa (Fig. 3b). One possible explanation for this is overestimated cooling by the large-scale advective tendency (Fig. 1b). Large-scale advective cooling is proportional to the sounding-derived rain rate based on Q_1. During 3–13 November, this sounding-derived rain rate was 5.17 mm day^{-1}, much greater than the 2.13 mm day^{-1} estimated by TRMM 3B42. Simulations with and without thermodynamic nudging had rain rates of 1.38 and 4.85 mm day^{-1}, respectively, during this period. This suggests that nudging may be compensating for errors in the advective tendency. The Research Vessel *Revelle* was at port during early November, reducing the NSA from four radiosonde sites to three, which could result in a less accurate advective forcing tendency.

Because of the imposed advective forcing, the time evolutions of the observed and simulated Q_1 and $-Q_2 C_p/L_v$ including nudging terms are very similar (Figs. 4a–d). The convectively active periods are characterized by top-heavy heating and drying profiles that peak near 400 hPa. The suppressed period, centered on 14 November, is characterized by small amounts of cooling and moistening. Figures 4e and 4f show the heat and moisture tendency from just the physics processes. There is considerably more cooling and moistening during the suppressed period (Figs. 4e,f), which may be more consistent with the exceptionally dry conditions (Fig. 2).
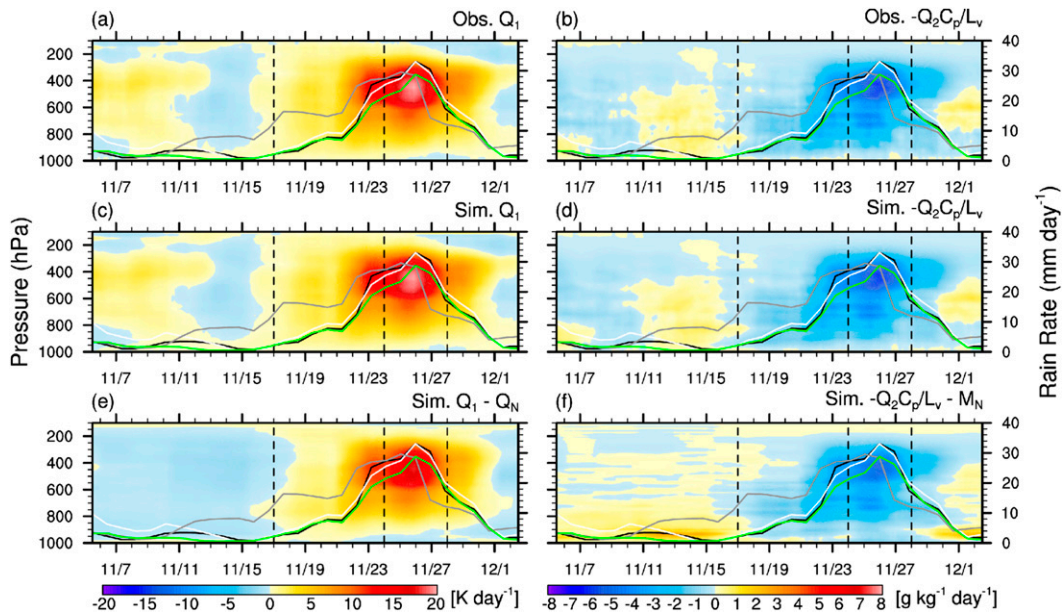
FIG. 4. Observed (a) Q_1 (K day^{-1}) and (b) $-Q_2 C_p/L_v$ (g kg^{-1} day^{-1}) and simulated (c) Q_1 (K day^{-1}) and (d) $-Q_2 C_p/L_v$ (g kg^{-1} day^{-1}). (e),(f) As in (c) and (d), but excluding nudging terms. Rain-rate convention follows Fig. 1b.

Figure 5 shows the simulated and S-Pol rain rates and area for the precipitating cloud types and weakly and nonprecipitating cloud, respectively, as well as the contributions of each cloud type to Q_1 and $-Q_2 C_p/L_v$ in the simulation. Nudging terms cannot be decomposed by cloud type and are excluded. Simulated heating from shallow convective clouds is concentrated between 700 and 900 hPa (Fig. 5a), while drying is concentrated below 800 hPa with a small amount of moistening near 700 hPa (Fig. 5b). The mismatch is due to eddy moisture transport, which produces moistening near 700 hPa and drying below 850 hPa. In congestus clouds, heating is caused by condensation and peaks between 600 and 800 hPa (Fig. 5c). Similar to shallow convection, the drying due to condensation near the top of the cloud is canceled out by eddy moisture transport (Fig. 5d). During the enhanced period, simulated deep convective clouds produce intense heating and drying through the depth of the free troposphere (Figs. 5e,f). Within stratiform clouds, heating and drying associated with deposition occurs at upper levels, while cooling and moistening due to reevaporation occurs at low levels (Figs. 5g,h). These heating and moistening profiles are broadly consistent with previous modeling (e.g., Johnson et al. 2002; Lang et al. 2003; Tao et al. 2003; Tulich et al. 2007) and observational studies (e.g., Johnson 1984; Yang and Smith 2000; Schumacher et al. 2007; Kodama et al. 2009; Hagos 2010). The apparent heat source Q_1 in the weakly and nonprecipitating cloud category (Fig. 5i), which includes

clear sky conditions, is dominated by radiation. Longwave cooling is greatest during the suppressed period and lowest during the enhanced period. Upper-level heating is also produced by ice deposition within anvil clouds. In addition, eddy transport by weakly and nonprecipitating shallow clouds produces moistening near 900 hPa (Fig. 5j).

Because of the thermodynamic nudging, the evolutions of the observed and simulated moisture tendencies are very similar. The simulation features low-level moistening during the suppressed and developing period followed by a stepwise transition to upper-level moistening around 17 November (Fig. 6a). This is followed by drying, which begins near the surface on 21 November and intensifies as it expands vertically, eventually encompassing most of the troposphere by the end of November.

Equation (4) can be rearranged so that

$$\frac{\partial q_v}{\partial t} = M_V + M_H - Q_2 C_p/L_v = M_C + M_H. \quad (5)$$

Here, M_C is the column-confined moisture tendency, introduced by Chikira (2014), which includes the large-scale vertical moisture advection M_V and $-Q_2 C_p/L_v$. This term is referred to as the column-confined moisture tendency because it includes all the processes that take place in a vertical column; it is not a vertically integrated quantity. The advantage of this rearrangement of terms is that it combines M_V and $-Q_2 C_p/L_v$, two large and
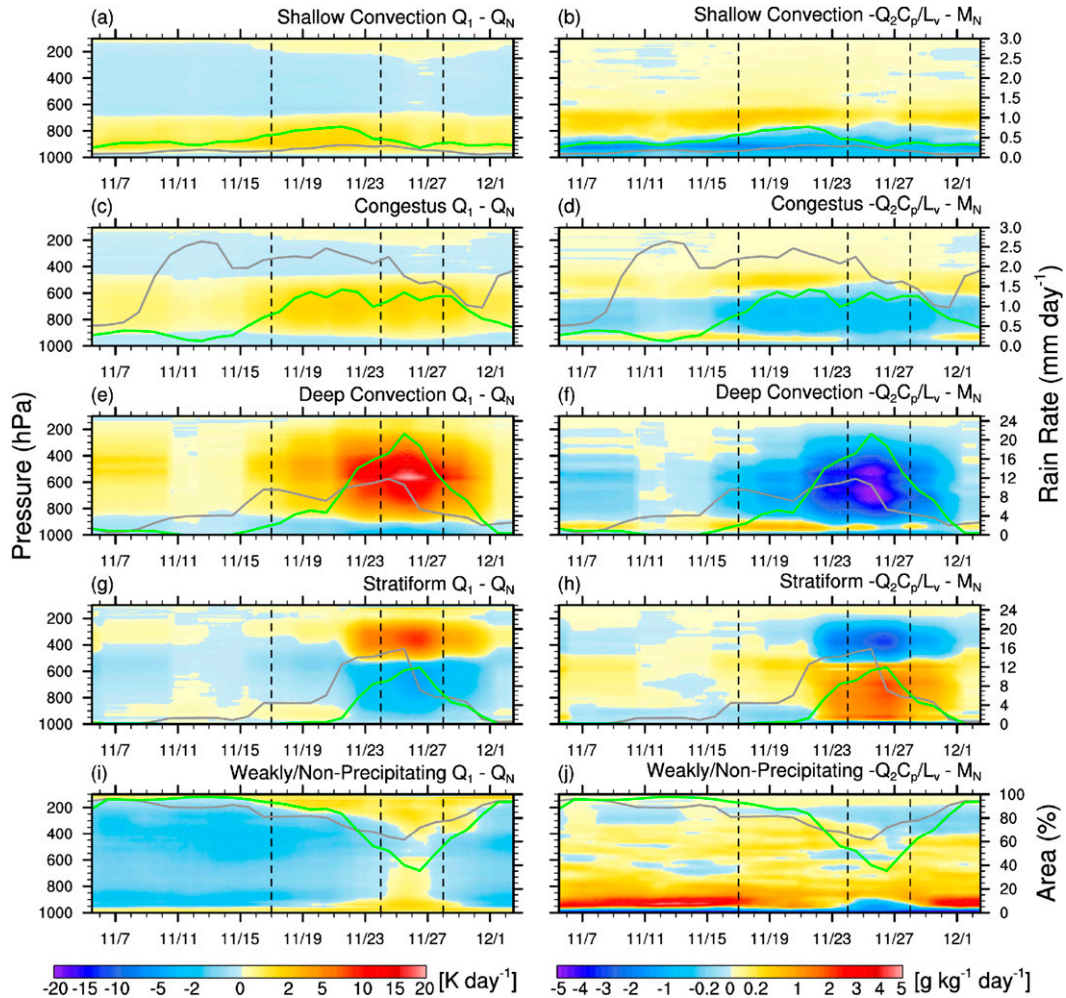
FIG. 5. The (left) $Q_1 - Q_N$ (K day^{-1}; shaded) and (right) $-Q_2 C_p/L_v - M_N$ (g kg^{-1} day^{-1}; shaded) for each cloud type and 1-km S-Pol (gray) and surface simulated (green) rain rate (mm day^{-1}) for (a),(b) shallow convection, (c),(d) congestus, (e),(f) deep convection, (g),(h) stratiform, and area (%) for (i),(j) weakly and nonprecipitating clouds. Unconditional averages are performed for each cloud type and include zeros when the cloud type is absent.

canceling terms, which, as will be shown in section 3b, are both closely related to clouds. The large-scale horizontal moisture advection is M_H.

Figure 6b shows the time evolution of M_C [Eq. (5)] using the observed M_V and simulated $-Q_2 C_p/L_v$. Most of the time tendency of moisture up through 21 November (Fig. 6a) is explained by M_C. That is because the moisture tendency due to large-scale horizontal advection is small during this period (Fig. 6c). Drying due to M_H shows a tilted signature (Fig. 6c) similar to that in the dissipating period (after 21 November in Fig. 6a) but with a much larger amplitude. M_C appears to be canceling out most of the drying associated with this large-scale horizontal advection. The focus of the remainder of this study will be on explaining the time

evolution of M_C, treating M_H as an external process. In the following section, M_V, which is a major component of M_C, is parameterized assuming a balance between diabatic heating and large-scale vertical potential temperature advection.

b. Contribution of physical processes and clouds to moisture

Numerous studies have shown that vertical motion in the deep tropics is closely related to diabatic heating. Under these conditions, both the weak temperature gradient (Sobel et al. 2001) and damped-wave or weak pressure gradient approximation (Kuang 2008; Romps 2012a,b) generally hold. Assuming a balance between diabatic heating and the large-scale vertical potential temperature
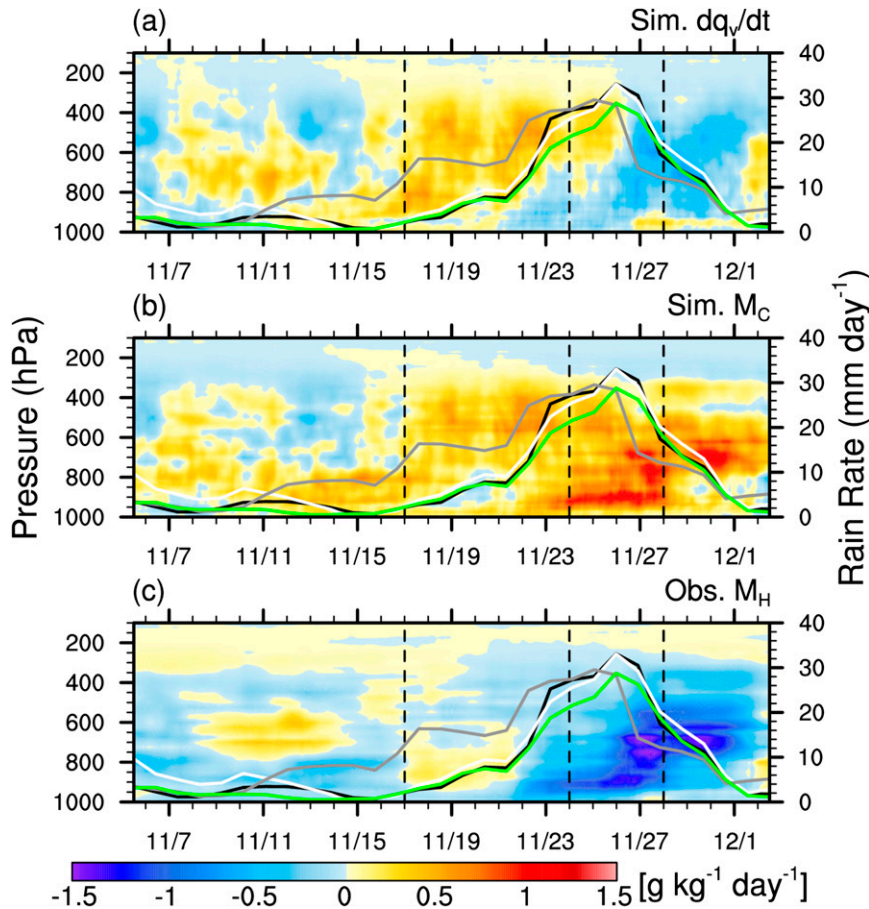
FIG. 6. Simulated (a) dq_v/dt and (b) M_C, and (c) observed M_H (g kg^{-1} day^{-1}; shaded). Rain-rate convention follows Fig. 1b.

advection, the domain-averaged vertical velocity w can be approximated as $w \approx -1/\overline{\pi}(\partial\overline{\theta}/\partial z)^{-1}Q_1$. The static stability and Q_1 can be taken from either observations or the simulation. Using this estimate of w, the large-scale vertical moisture advection assuming diabatic balance can be expressed as

$$M_{V\mathrm{DB}} \equiv -1/\overline{\pi}(\partial\overline{q}_v/\partial z)(\partial\overline{\theta}/\partial z)^{-1}Q_1. \qquad (6)$$

Adding $-Q_2C_p/L_v$ to $M_{V\mathrm{DB}}$ yields an approximation of the column-confined moisture tendency M_C assuming diabatic balance:

$$M_{C\mathrm{DB}} \equiv M_{V\mathrm{DB}} - Q_2C_p/L_v. \qquad (7)$$

The quantity $M_{V\mathrm{DB}}$ can also be expressed as $M_{V\mathrm{DB}} = \overline{\alpha}(L_V/C_p)Q_1$, where $\alpha \equiv -1/\overline{\pi}(C_p/L_v)(\partial\overline{q}_v/\partial z)(\partial\overline{\theta}/\partial z)^{-1}$ is an efficiency parameter that describes the amount of large-scale vertical moisture advection for a given amount of heating (Chikira 2014). Only domain averages of α are used in the calculation of $M_{V\mathrm{DB}}$ and $M_{C\mathrm{DB}}$ since the vertical velocity resulting from heating is

meant to represent the effects of large-scale gravity wave adjustment occurring over the entire domain.

Figures 7a and 7c show the observed vertical velocity and the diabatic balance approximation using simulated static stability and Q_1. Similarly, Figs. 7b and 7d show the observed M_V and its diabatic balance approximation $M_{V\mathrm{DB}}$ using simulated fields. The analysis is limited to above 950 hPa, because, as one approaches the surface, boundary layer effects become important and the diabatic heating and static stability can no longer be used to estimate the large-scale vertical velocity (Raymond and Zeng 2005; Wang et al. 2013). Both the observed vertical velocity and that approximated using diabatic balance are greatest during the enhanced phase and peak between 200 and 300 hPa (Figs. 7a and 7c). The observed and diabatic balance approximation of the large-scale vertical moisture advection are less top heavy since the vertical moisture gradient is greatest at low levels (Figs. 7b,d). The horizontal stripes apparent in the observed M_V (Fig. 7d) are absent in $M_{V\mathrm{DB}}$ (Fig. 7d); this is because $M_{V\mathrm{DB}}$ is not dependent on Q_2 [Eq. (6)].
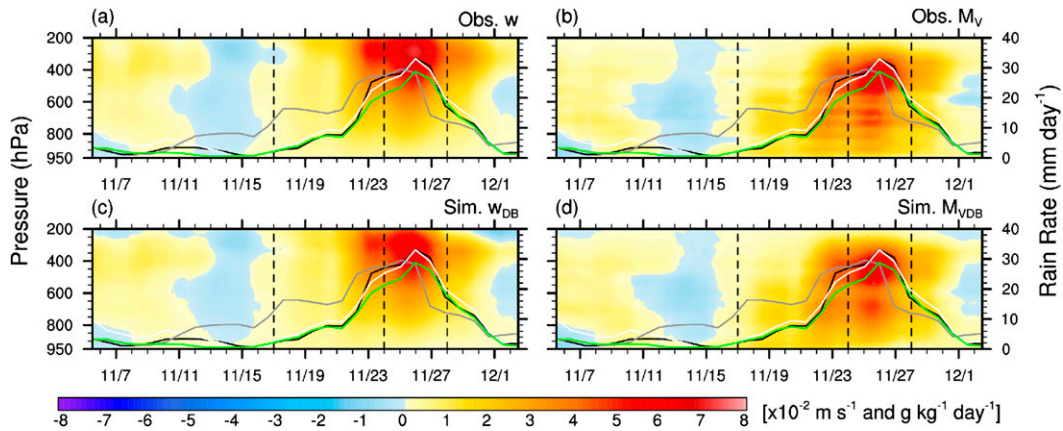
FIG. 7. Observed (a) vertical velocity ($\times 10^{-2}$ m s^{-1}) and (b) vertical moisture advection (g kg^{-1} day^{-1}), and the simulated (c) vertical velocity ($\times 10^{-2}$ m s^{-1}) and (d) vertical moisture advection (g kg^{-1} day^{-1}) approximated using diabatic balance. Rain-rate convention follows Fig. 1b.

Vertical moisture advection M_V is a large component of the large-scale moisture advection in Fig. 1a and also contains the same horizontal striping pattern because of the temporal and vertical variability of this field. In contrast, $M_{V\text{DB}}$ is derived from the more smoothly varying simulated diabatic heating (Fig. 4a) and vertical moisture gradient and does not contain these horizontal stripes.

The similarity of M_C (Fig. 6b) and M_{CDB} (Figs. 8a) suggests that M_{CDB} can be partitioned into contributions from different terms and cloud types using the model output. Figures 8b and 8c show the contributions from physics processes $M_{\text{CDB-PYS}}$ and thermodynamic nudging $M_{\text{CDB-}N}$ to M_{CDB}. This is calculated by decomposing Q_1 and $-Q_2 C_p/L_v$ [Eqs. (3) and (4)] within Eq. (7) to the components that exclude Q_N and M_N and only include these nudging terms. Fig. 8b shows that physics processes are responsible for the stepwise transition from low-level to upper-level moistening between the suppressed and developing phases in M_{CDB} (Fig. 8a). The contribution from thermodynamic nudging $M_{\text{CDB-}N}$ is responsible for mid- and upper-level moistening during the suppressed phase (Fig. 8c), which may be associated with the errors in the sounding array budget discussed earlier. The horizontal stripes apparent in Fig. 8 are a result of temporal averaging being applied to a field with occasional high magnitude values associated with short-lived bursts of convection. During these bursts of convection the diabatic balance assumption may break down even though it captures the overall behavior during the four periods. The stripes do not have a preference for a particular level.

In addition to variations in diabatic heating and moistening, changes in the thermodynamic environment represented by α also affect M_{CDB}. The profiles of observed

and simulated α averaged over 3 November–5 December (Fig. 9a) closely resemble those in Chikira (2014) (their Fig. 12a). Similar to Chikira (2014), we also find that α decreases with height because of the decrease in $\partial q_v/\partial z$ with height. Approaching the surface, values of α sharply increase because of the very low values of $\partial\theta/\partial z$ near the surface. However, as was mentioned earlier, boundary layer effects become important near the surface, and the assumption of diabatic balance no longer holds.

For illustrative purposes, let us consider a simplified version of Eq. (7) where only condensation and evaporation take place; the equation reduces to $(c - e)(\alpha - 1)$ (Chikira 2014). In this case, values of α greater (less) than one are associated with net moistening (drying) when there is condensation. Fig. 9a shows that $\alpha = 1$ near 625 hPa just below the melting level (dashed line) at 575 hPa. Above the melting level, deposition occurs that produces additional heat release because of the latent heating of freezing. However, the effect of additional latent heating is quickly overwhelmed by the decrease in $\partial q_v/\partial z$ with height.

Figure 9b shows the simulated α anomalies (shaded) and total values (contours). When α is anomalously large (small) diabatic heating is particularly efficient (inefficient) at generating moistening through large-scale vertical advection. At midlevels, positive α anomalies are observed in the developing phase and negative α anomalies occur in the dissipating phase. This behavior is due to the tilted moisture anomaly centered on the enhanced phase (Fig. 2b). Positive (negative) α anomalies are also observed at upper levels during the enhanced (suppressed) phase. In general, α and $\partial q_v/\partial z$ increase with the value of q_v so that α anomalies at this level have the same sign as the moisture anomalies (Fig. 2b). The level where $\alpha = 1$ varies from 550 to 700 hPa.
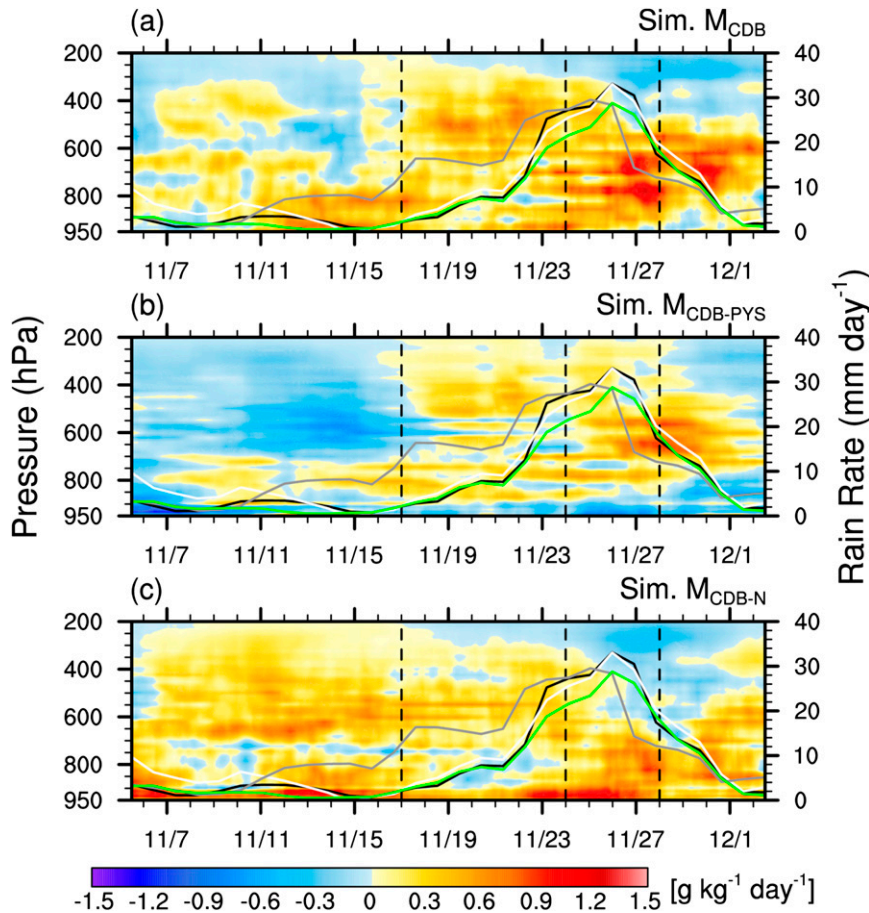
FIG. 8. Simulated (a) M_{CDB}, (b) $M_{CDB-PYS}$, and (c) M_{CDB-N} (g kg^{-1} day^{-1}). Rain-rate convention follows Fig. 1b.

The importance of different cloud types and physical processes (microphysics, eddy transport, and radiation) to the time evolution of moisture can be expressed by partitioning $M_{CDB-PYS}$ (Fig. 8b) into the components associated with each cloud type and process.

The contribution of microphysics to M_{CDB} can be expressed as

$$M_{CDB-M} = \overline{\alpha}(L_V/C_p)Q_M + M_M. \qquad (8)$$

Discarding the diffusion and horizontal eddy flux convergence terms, which are negligible, the equation for
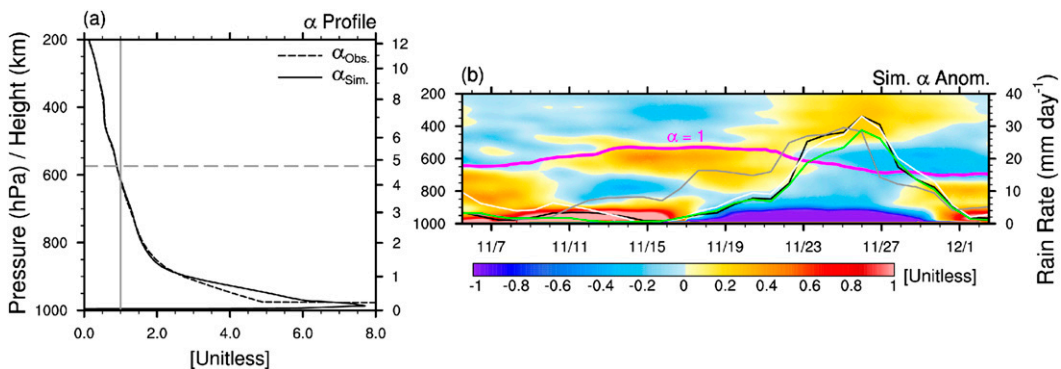
FIG. 9. (a) Average value of observed and simulated α (unitless) and (b) simulated α anomalies (unitless; shaded) and the total value of α (contoured in magenta at 1.0). In (a), the horizontal and vertical lines indicate the freezing level and $\alpha = 1$, respectively. In (b), anomalies are with respect to the 3 Nov–5 Dec mean. Rain-rate convention follows Fig. 1b.

the M_{CDB} tendency due to eddy transport can be expressed as

$$M_{CDB-E} = \overline{\alpha}(L_V/C_p)\overline{\pi}\left(-\frac{1}{\overline{\rho}}\frac{\partial\overline{\rho}w'\theta'}{\partial z}\right) - \frac{1}{\overline{\rho}}\frac{\partial\overline{\rho}w'q_v'}{\partial z}. \quad (9)$$

Last, the simulated M_{CDB} tendency due to radiation can be expressed as

$$M_{CDB-R} = \overline{\alpha}(L_V/C_p)Q_R, \quad (10)$$

where Q_R can be partitioned into both longwave Q_{LW} and shortwave Q_{SW} contributions. These moisture tendencies can also be separated into contributions from different cloud types. For example, M_{CDB-M} due to deep convection is calculated by averaging Q_M and M_M over the whole domain after setting grid points without deep convection to zero.

The left and center columns of Fig. 10 show the time evolution of M_M and M_{VDB-M}, the second and first terms in Eq. (8), respectively; the right column shows their sum, M_{CDB-M}. Contributions of weakly and non-precipitating clouds, shallow convection, congestus, and deep convection to M_M are dominated by drying, which peaks at 950, 900, 700, and 600 hPa, respectively (Figs. 10a,d,g,m). Stratiform is characterized by drying aloft and moistening below the melting level because of the reevaporation of rainwater (Fig. 10j). The panels in the right column show that there are large cancellations between M_M and M_{VDB-M}. However, because of the higher values of α at low levels, when the two terms are added together, moistening due to M_{CDB-M} occurs below 700 hPa for cloud types with low-level condensation. The exception is stratiform cloud (Fig. 10l). When reevaporation occurs at low levels, where α is greater than one, the direct moistening from reevaporation (Fig. 10j) is overwhelmed by the drying effect of evaporative-cooling-induced subsidence (Fig. 10k). Melting graupel and snow in deep convective and stratiform clouds produce cooling, which results in subsidence and the drying peaks near 600 hPa (Figs. 10i,l). Liquid–ice transitions were also found to have a major drying effect at midlevels in Chikira (2014).

Figure 11 shows the moisture tendency due to the eddy transport processes. In shallow convection, the second term in Eq. (9), the eddy moisture transport M_E produces moistening near 800 hPa and drying below 925 hPa (Fig. 11a). Shallow convection in the simulation is characterized by a positive vertical eddy moisture flux $w'q_v'$ anomaly, near 800 hPa. As a result, eddy moisture flux convergence and divergence occur above and below this level. Congestus and deep convection are characterized by deeper updrafts producing an elevated $w'q_v'$

anomaly, which explains why the dipole of moistening is located at higher altitudes (Figs. 11d,g). Moistening above 500 hPa in deep convection is greatest during the developing period; this appears to be associated with more top-heavy vertical velocity profiles during the developing period (not shown). Weakly and non-precipitating clouds are best characterized as a shallower version of the precipitating shallow convection, and their moistening peak occurs near 950 hPa (Fig. 11m). When summed together, the eddy moisture transport in these four cloud types resembles that for convective clouds in Xu (1995). The moistening at 800 hPa due to M_E in stratiform regions (Fig. 11j) is associated with a negative $w'q_v'$ anomaly resulting from downdrafts. Xu (1995) also found moistening from eddy transport at this level as well as a couplet of drying over moistening centered near the melting level and weak eddy moistening near 300 hPa. The total moistening due to M_E is greatest at low levels in the suppressed period and rapidly transitions to a top-heavy moistening profile during the developing period (Fig. 11p).

The first term in Eq. (9), M_{VDB-E}, is much smaller than the second, M_E. With the exception of deep convection and weakly and nonprecipitating clouds (Figs. 11h,n) its effect is negligible. Profiles of eddy heat transport Q_E, which is used to calculate M_{VDB-E} for the various cloud types, are also similar to those in Xu (1995). The low-level drying in deep convection is associated with a positive $w'\theta'$ anomaly near 600 hPa that produces upper-level warming and moistening and low-level cooling and subsidence (Fig. 11h). Weakly precipitating shallow clouds are associated with a positive $w'\theta'$ anomaly near 900 hPa producing a similar dipole of moistening over drying (Fig. 11n). Overall, the evolution of M_{CDB-E} for each cloud type is much more similar to M_E than M_{VDB-E}, illustrating the importance of M_E.

Despite the fact that deep convective updrafts are much stronger than those in congestus and shallow convection (Schumacher et al. 2015), the magnitude of the moistening by eddy transport is remarkably similar for these cloud types. This is because the maximum intensity of water vapor anomalies is much lower at the altitude where deep convective updrafts peak due to the lower saturation mixing ratio.

Figure 12 shows the contributions of shortwave and longwave radiation to M_{CDB-R} [Eq. (10)]. Only the total fields are shown since most of the variability occurs within the weakly and nonprecipitating cloud type because of the extensive area coverage of this type. The suppressed period, centered on 15 November, is characterized by longwave cooling, which results in drying (Fig. 12a), and shortwave heating, which results in moistening (Fig. 12b). During the enhanced period,
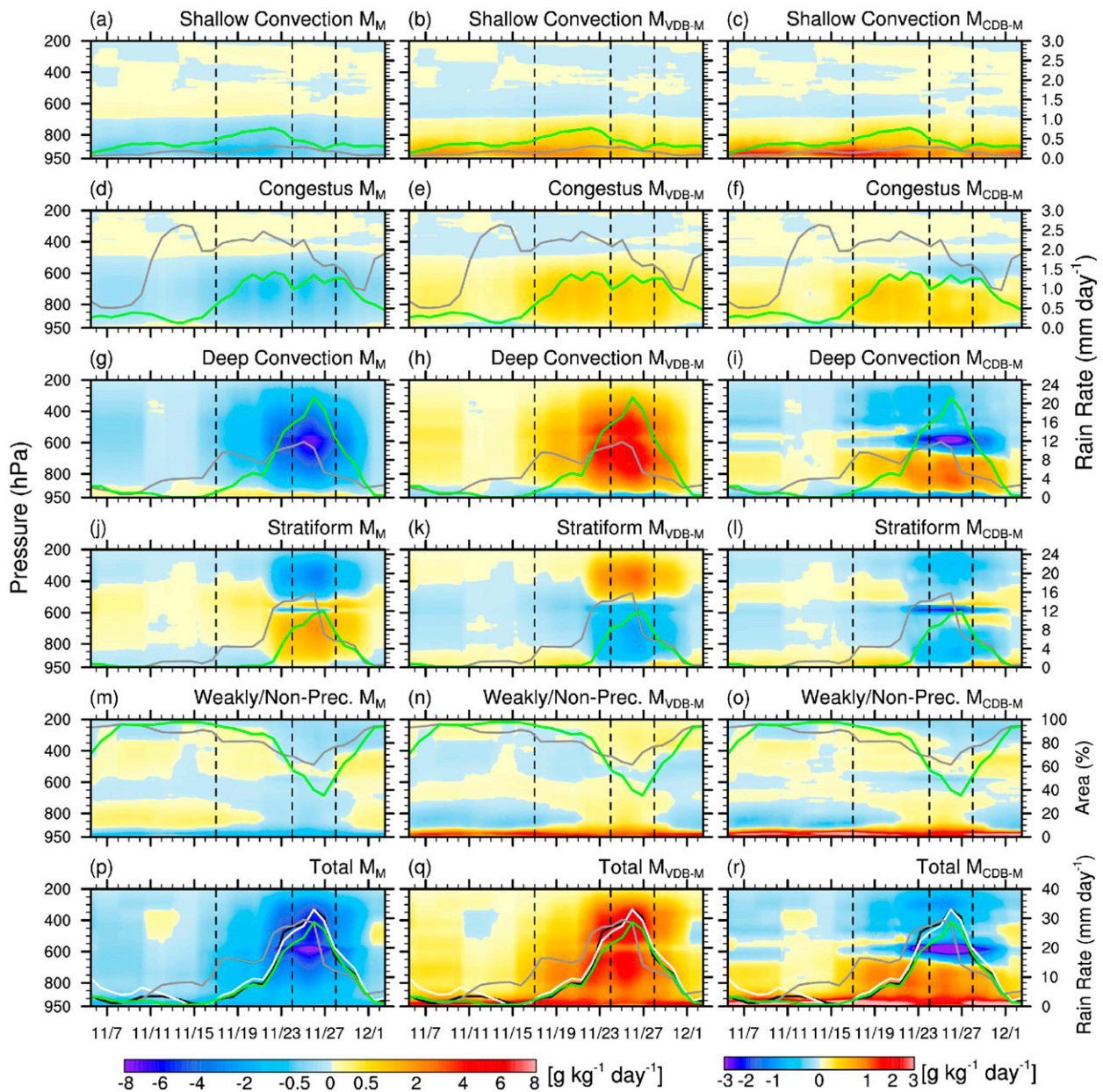
FIG. 10. The (left) M_M, (center) M_{VDB-M}, and (right) M_{CDB-M} (g kg^{-1} day^{-1}) for (a)–(c) shallow convection, (d)–(f) congestus, (g)–(i) deep convection, (j)–(l) stratiform, (m)–(o) weakly and nonprecipitating clouds, and (p)–(r) all points. Rain rate and area in (a)–(o) follow Fig. 5. Rain-rate convention in (p)–(r) follows Fig. 1b.

increased cloud cover results in additional longwave trapping and reduced drying. Shortwave heating and moistening is also reduced, but this is canceled out by the longwave effect (Fig. 12c). Chikira (2014) also found that reduced longwave cooling within the MJO convective envelope produces midlevel moistening. However, in contrast to Fig. 12c, that study suggested that radiation has little effect above 400 hPa. In addition, Chikira (2014) estimated that radiation plays a more important role in moistening the midlevels of the MJO

convective envelope than the eddy transport, while our results suggest the opposite.

The combined effect of microphysics, eddy flux convergence, and radiation on M_{CDB} is shown in Fig. 13. Anomalies with respect to the time mean are also shown to emphasize the contrasts between the steady-state moistening from each cloud type and the temporal variations responsible for the growth of the MJO moisture anomaly. Shallow convection produces moistening between 650 and 925 hPa (Fig. 13a) and a peak moistening anomaly of
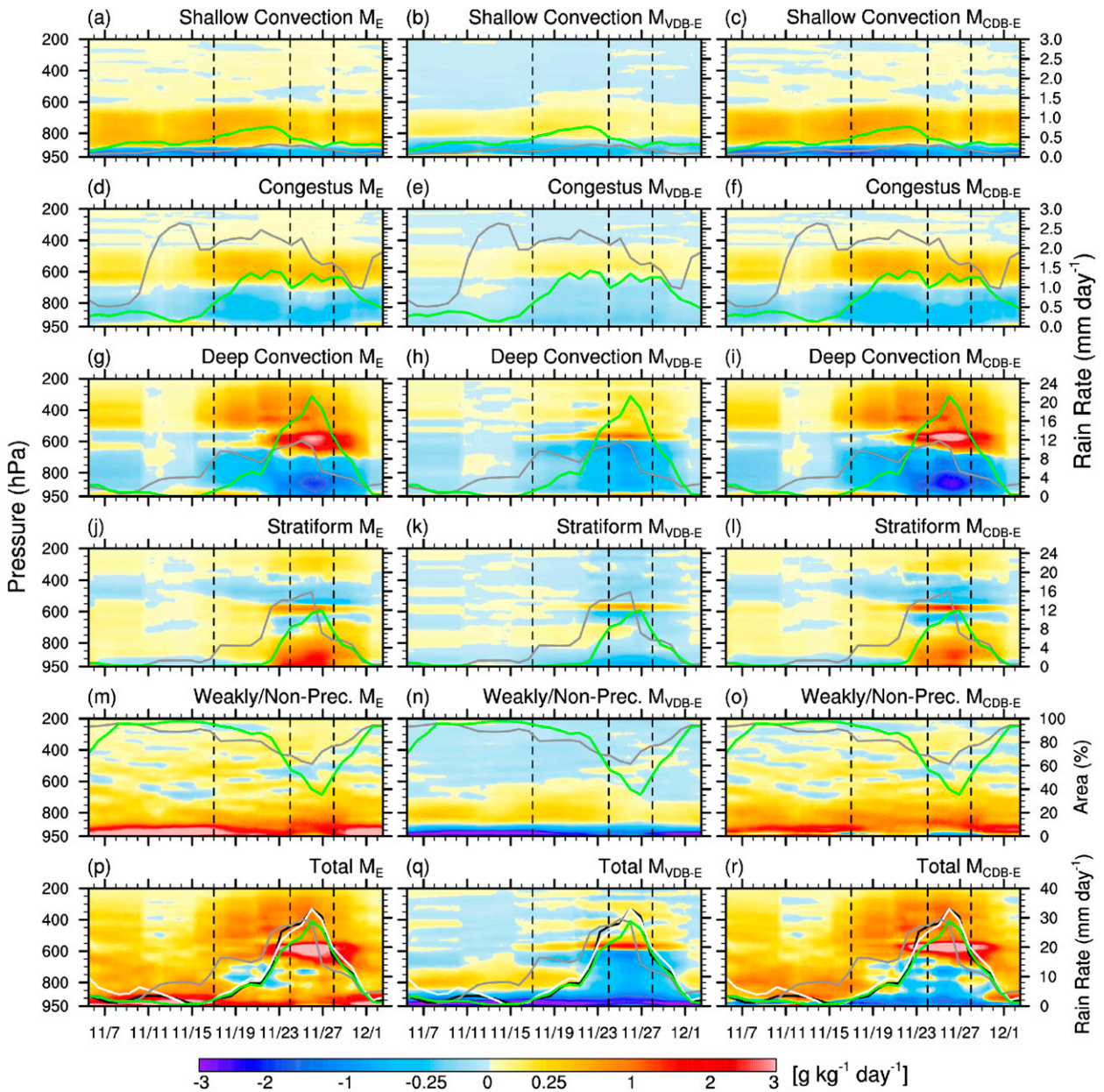
FIG. 11. As in Fig. 10, but for (left) M_E, (center) M_{VDB-E}, and (right) M_{CDB-E} (g kg^{-1} day^{-1}) for (a)–(c) shallow convection, (d)–(f) congestus, (g)–(i) deep convection, (j)–(l) stratiform, (m)–(o) weakly and nonprecipitating clouds, and (p)–(r) all points.

0.2 g kg^{-1} day^{-1} on 17 November, several days before the peak rain rate from this cloud type (Fig. 13b). Figure 13b shows that shallow convection makes a substantial contribution to low-level moistening associated with the MJO but does not show that the transition to midlevel and upper-level moistening from congestus and deep convection is an inevitable outcome of the presence of shallow convection. Previous studies have suggested that shallow convection can exist in a steady state being balanced by the subsidence and drying associated with radiative cooling (Emanuel et al. 2014). The shallow

convection category includes a wide range of cloud morphologies: isolated cells and those connected to convective systems and shallow clouds that develop into congestus and deep convection and those that do not. Changes in the relative amount and properties of these shallow convection subtypes may help explain the peak in moistening on 17 November (Fig. 13b); we leave this to future studies.

The total moistening from shallow convective clouds is larger and more uniform in time than the moistening from congestus clouds (Figs. 13a,c), but the magnitudes
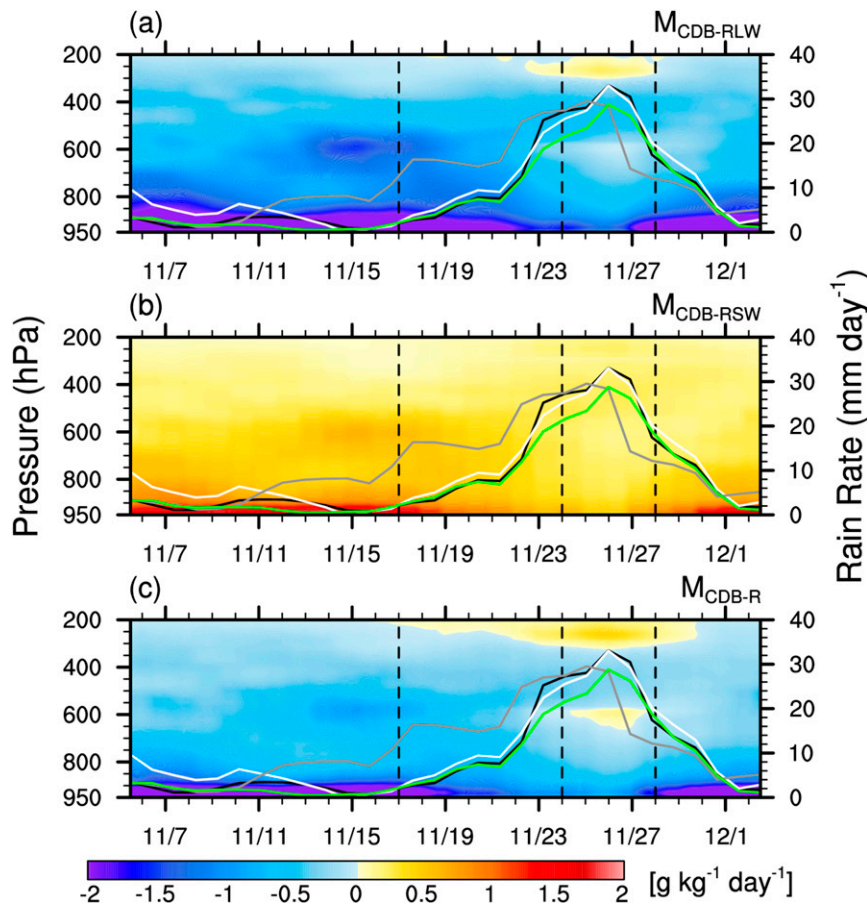
FIG. 12. The (a) $M_{CDB\text{-}R\mathrm{LW}}$, (b) $M_{CDB\text{-}R\mathrm{SW}}$, and (c) $M_{CDB\text{-}R}$ (g kg^{-1} day^{-1}). Rain-rate convention follows Fig. 1b.

of the moistening anomalies are similar (Figs. 13b,d). The congestus moistening anomaly is strongest between 500 and 600 hPa and follows the shallow convective moistening anomaly by several days. The total moisture tendency resulting from deep convection is characterized by upper-level moistening and low-level drying (Fig. 13e). For this cloud type, there is a large amount of cancellation between $M_{CDB\text{-}M}$ and $M_{CDB\text{-}E}$. The drying aloft due to $M_{CDB\text{-}M}$ (Fig. 10i) is overwhelmed by moistening due to $M_{CDB\text{-}E}$ (Fig. 11i), which is itself dominated by M_E (Fig. 11g). The opposite occurs at low levels; moistening due to $M_{CDB\text{-}M}$ is overwhelmed by drying due to $M_{CDB\text{-}E}$.

Stratiform is characterized by drying throughout the free troposphere (Fig. 13g). Both stratiform and deep convective clouds are characterized by upper-level drying due to $M_{CDB\text{-}M}$ (Figs. 10i,l). However, within stratiform clouds $M_{CDB\text{-}E}$ is weak at upper-levels (Fig. 11l) and unable to counteract the drying due to $M_{CDB\text{-}M}$ (Fig. 10l). This is due to the presence of very weak updrafts in the stratiform clouds consistent with

modeling (Del Genio et al. 2012) and observational (Schumacher et al. 2015) studies.

Weakly and nonprecipitating clouds are characterized by anomalous drying, particularly at midlevels, during the suppressed period and also by anomalous moistening, particularly at low levels, during the enhanced period (Fig. 13j). Condensation (Fig. 10o) and eddy moisture transport (Fig. 11o) within weakly and nonprecipitating shallow clouds are responsible for the sliver of low-level moistening in Fig. 13i; however, when the time mean is removed, this moistening is less apparent. Long-term observational studies also suggest that shallow clouds are much more weakly modulated by the MJO than other cloud types (Deng et al. 2013; Barnes and Houze 2013). The results of this study suggest that this is especially true for the weakly and nonprecipitating shallow clouds. However, the difficulty of accurately simulating these clouds at such a coarse resolution should be emphasized.

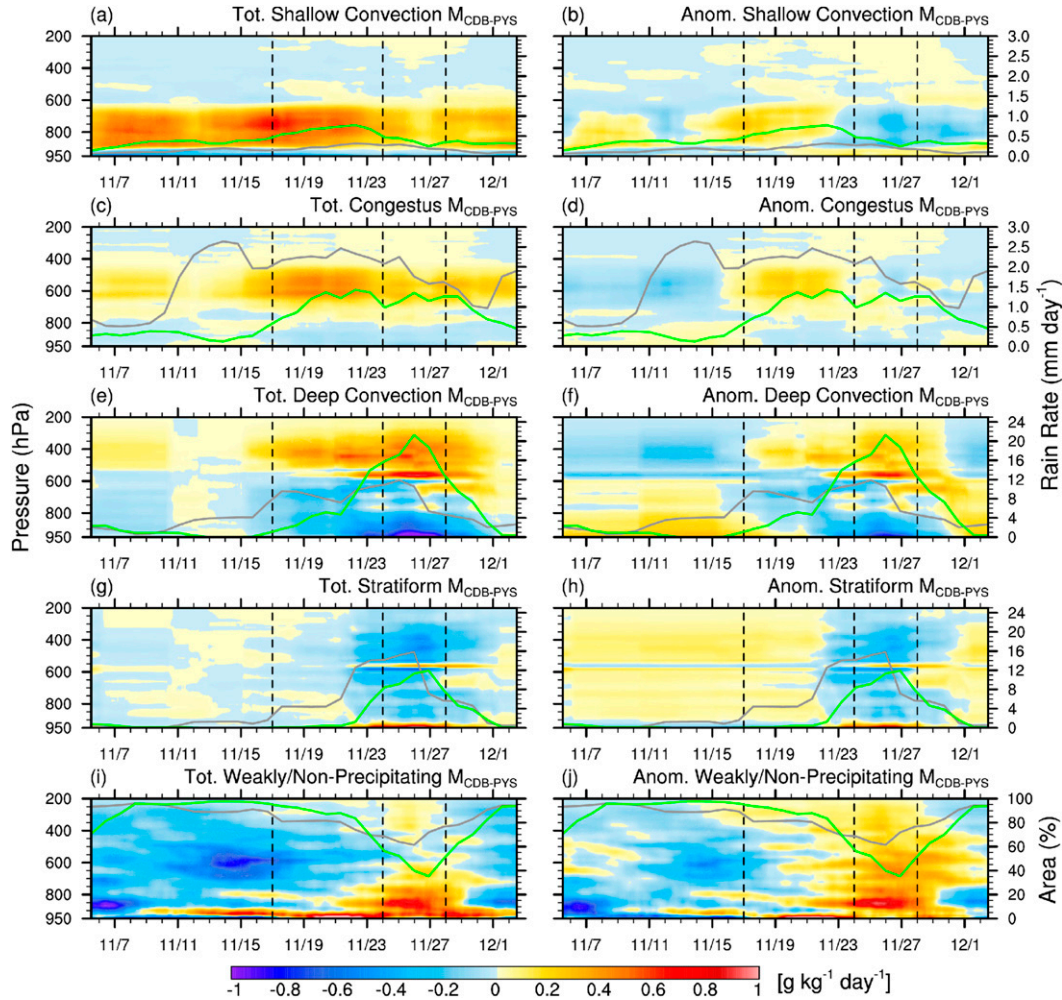To better quantify these results, Fig. 14 shows anomalies of the vertically integrated moisture tendencies

FIG. 13. (left) Total $M_{\text{CDB-PYS}}$ and (right) $M_{\text{CDB-PYS}}$ anomalies (g kg^{-1} day^{-1}) for (a),(b) shallow convection, (c),(d) congestus, (e),(f) deep convection, (g),(h) stratiform, and (i),(j) weakly and nonprecipitating clouds. Rain rate and area time series show total values following Fig. 5.

from various terms, including a subdivision by cloud type for $M_{\text{CDB-}M}$ and $M_{\text{CDB-}E}$, for three layers and each period. The lowest layer only extends down to 900 hPa, since the assumption of diabatic balance becomes questionable below this level. The residual is the difference between the observed dq_v/dt and the individual terms. In each panel, the two largest moistening and drying terms are highlighted in blue and red, respectively, with the largest of each in bold. In addition, the panel where each term experiences its largest absolute value is indicated by an underlined number. During the suppressed period, the two largest moistening terms at low levels are deep convective eddy transport and horizontal advection. The mean total value of each term during 3 November–5 December is negative; however, the reduction of a large drying term can produce anomalous moistening too. Deep convective eddy transport clearly plays a major role

in the onset of upper-level moistening during the developing and enhanced periods. During the dissipating period, the most important term is the large-scale horizontal advection, which dries out all three layers.

4. Summary and discussion

In this study, a cloud-resolving model (CRM) forced by observed large-scale advective tendencies was used to examine the contributions of specific cloud types and physical processes to the evolution of the vertical structure of moisture during the second MJO event of the DYNAMO campaign. Following Chikira (2014), the direct or cloud-scale effect of various cloud types and physical processes on $-Q_2 C_p/L_v$ was combined with the indirect effect on large-scale vertical moisture advection associated with diabatic heating.

	Suppressed			Developing			Enhanced			Dissipating		
300–500 hPa	-0.176	0.000	-0.001	0.698	0.001	0.006	0.274	0.000	-0.001	-0.511	0.000	-0.002
	0.134	-0.001	-0.036	0.125	0.004	0.087	0.028	-0.002	-0.013	-0.405	-0.002	-0.008
	0.119	0.193	-0.517	0.066	-0.422	0.917	-0.233	-0.272	0.943	-0.187	0.185	-0.409
	-0.026	0.090	0.037	-0.062	0.078	-0.042	0.144	-0.527	-0.118	0.026	0.039	0.037
	-0.123	-0.010	-0.017	-0.179	0.031	0.054	0.366	-0.050	0.000	0.218	0.017	-0.018
500–700 hPa	-0.213	0.000	-0.035	0.798	-0.005	0.109	0.026	0.004	-0.068	-0.441	0.003	-0.001
	0.435	-0.004	-0.235	0.464	0.142	0.326	-0.549	-0.140	0.176	-1.014	-0.054	0.040
	0.017	0.468	-0.512	0.062	0.378	-0.702	-0.255	-2.440	2.891	0.025	0.078	0.076
	-0.216	0.144	-0.044	-0.115	-0.031	0.078	0.683	-0.737	0.155	0.145	0.159	-0.077
	-0.156	0.007	-0.004	0.057	-0.005	0.034	0.030	-0.050	0.072	0.222	0.020	-0.068
900–700 hPa	0.017	-0.021	0.035	0.494	0.223	0.138	-0.635	-0.210	-0.318	-0.160	-0.061	-0.027
	0.264	-0.163	0.205	0.816	0.356	-0.326	-1.736	0.094	-0.044	-0.381	-0.085	-0.057
	-0.010	-0.429	0.846	-0.501	0.187	-0.585	0.603	1.395	-2.697	0.188	-0.116	0.426
	-0.231	0.156	-0.268	-0.008	0.149	-0.139	0.926	-0.863	1.130	-0.070	0.032	0.031
	-0.075	-0.117	-0.126	-0.146	0.154	0.013	0.405	0.342	0.186	0.090	-0.114	0.131

Key (kg m⁻² day⁻¹)

dq_v/dt	$M_{CDB-M-SH}$	$M_{CDB-E-SH}$
M_H	$M_{CDB-M-CN}$	$M_{CDB-E-CN}$
M_{CDB-N}	$M_{CDB-M-DC}$	$M_{CDB-E-DC}$
M_{CDB-R}	$M_{CDB-M-ST}$	$M_{CDB-E-ST}$
Residual	$M_{CDB-M-WP}$	$M_{CDB-E-WP}$

FIG. 14. Anomalies (with respect to the 3 Nov–5 Dec mean) of the moisture tendency terms in the key integrated over the indicated layer during each period (see Fig. 1) (kg m⁻² day⁻¹). The residual is the difference between dq_v/dt and the sum of the individual terms. The contribution of each cloud type is shown to (center) the microphysical [Eq. (8)] and (right) eddy flux convergence [Eq. (9)] column-confined moisture tendency. (top)–(bottom) The cloud types within these columns are shallow convection (SH), congestus (CN), deep convection (DC), stratiform (ST), and weakly and nonprecipitating clouds (WP). The two largest moistening and drying anomalies within each panel are highlighted red and blue, respectively, and the largest of each is in bold. The panel with the largest absolute value of each term is indicated by underlined values.

Figure 15 summarizes the key processes responsible for the evolution of moisture within the simulation during the suppressed, developing, enhanced, and dissipating phases of local MJO convective activity. The suppressed period was characterized by reduced rain rates and midlevel water vapor and low-level moistening largely captured by the column-confined moisture tendency M_{CDB}. The tendency M_{CDB} represents the sum of $-Q_2 C_p/L_v$ and the large-scale vertical moisture advection, which is estimated using Q_1 and an efficiency parameter α assuming diabatic balance. Analysis of M_{CDB} showed that low-level moistening during the suppressed period has large contributions from the vertical eddy moisture transport by shallow convective clouds. However, this may be dependent on the resolution of the simulation and how cloud types are identified. The arrows in Fig. 14 illustrate the magnitude and orientation of $\overline{w'q_v'}$. Eddy moisture flux convergence and moistening occurs at the head of the vector, while divergence and drying occurs at the tail. Condensation within warm clouds (indicated by solid blue dots) also acts to moisten low levels because the ascent associated

with the heating advects more moisture than is removed by condensation. This is because of the large vertical moisture gradient at low levels, which allows a small amount of heating to produce a large amount of large-scale vertical moisture advection. Midlevel drying due to radiative-cooling-induced subsidence is also present during this period.

Increased convective activity during the developing phase coincided with a stepwise transition from low-level to mid- and upper-level moistening largely captured by M_{CDB}. Midlevel moistening was partly due to condensation within congestus clouds and vertical eddy moisture flux convergence at their tops. Moistening above 500 hPa was primarily due to eddy moisture transport associated with deep convection that overwhelms the drying associated with ice processes.

The dissipating period was characterized by a relatively high stratiform rain fraction. Ice deposition in stratiform clouds heats and removes moisture from the upper troposphere. As in deep convection, because of the low value of α aloft, the heating-induced moisture advection only partially cancels out the direct removal
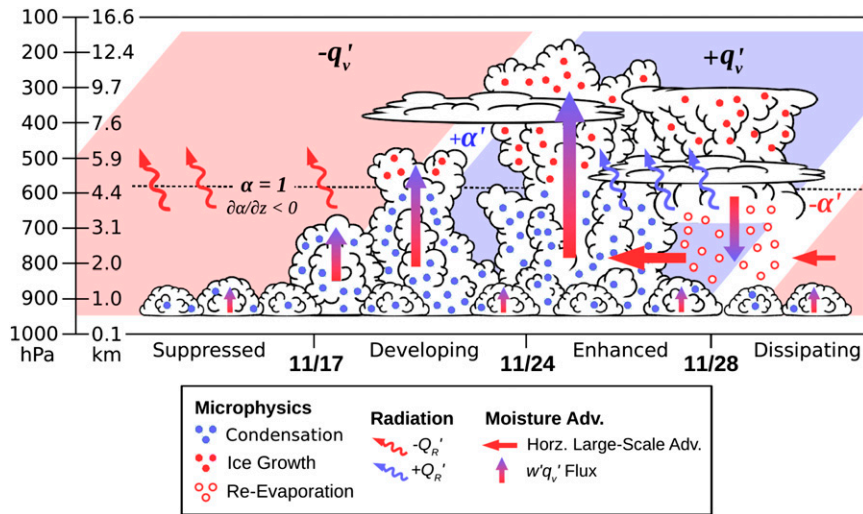
FIG. 15. Summary of the contribution of different physical processes and cloud types to the evolution of moisture in the simulated MJO event. Red (blue) indicates processes that dry (moisten). The $w'q'_v$ vectors indicate the orientation of the moisture flux, while the shading indicates either moisture flux convergence (blue) or divergence (red).

of moisture. However, in contrast to deep convection, upper-level moistening by eddy moisture transport is weak in stratiform clouds, so the net effect of stratiform on M_{CDB} is to dry these levels. Large-scale horizontal advection produces significant dry air advection, which begins at low levels and builds upward; however, this process is not included in M_{CDB}. Because the low levels dry before the upper levels, the midlevel value of α is depressed during this period, making the diabatic heating less efficient at generating vertical moisture advection.

The temporal coincidence of low-level moistening and relatively shallow clouds during the developing phase of the MJO has led many studies to infer that these clouds are responsible for this low-level moistening (Johnson et al. 1999; Kemball-Cook and Weare 2001; Benedict and Randall 2007; Thayer-Calder and Randall 2009) and could possibly be a precondition for the development of deep convection. However, observational studies reveal that convective deepening on small spatial scales can occur very quickly, and the direct moistening from these clouds does not appear to be a deciding factor (Hohenegger and Stevens 2013; Masunaga 2013). Instead, these studies attribute the moistening required for convective development to large-scale ascent. However, in the context of the MJO, a much larger and longer-time-scale process, large-scale ascent is almost entirely due to the heating within clouds. At these scales, shallow clouds are especially efficient at moistening because the amount of moistening for a given amount of heating is much greater at low levels than aloft (Chikira 2014). However, consistent with Deng et al. (2013) and Barnes

and Houze (2013), we found that precipitating and nonprecipitating shallow convection and their moistening are fairly constant in time.

Recent studies have also suggested that nonprecipitating cirrus and anvil clouds could also play a key role in the moistening observed during the developing period by reducing radiative cooling (Chikira 2014; Wang et al. 2015), consistent with our results. Although the focus of this study was on the developing period, our results also suggest that stratiform clouds are important to the discharge of moisture by the MJO. Therefore, the onset of widespread stratiform could be key to the time scale on which MJO moisture anomalies dissipate.

It should be noted that numerous processes that could trigger a transition from shallow to deep convection are observed during MJO events; this includes cold pools, 2-day waves, and extratropical activity. Therefore, our results do not imply that the transition from shallow to deep convection is an unavoidable outcome of eddy moisture transport by shallow convective and congestus clouds. Instead, the results of this study should merely be taken as an accounting of the relative importance of each physical process and cloud type to the intraseasonal time-scale moistening observed during the passage of the MJO convective envelope.

Klingaman et al. (2015) found that the moisture tendency as a function of rain rate over the equatorial Indian and Pacific Oceans is an excellent predictor of MJO forecast skill, which highlights the importance of understanding moisture–convection interactions. The vertical velocity in CRM simulations is highly sensitive

to microphysical parameterization and model resolution (Varble et al. 2014), which is likely to affect the vertical eddy moisture transport. Ice clouds, which indirectly affect the moisture tendency through their effects on radiation and large-scale ascent, are also a major uncertainty in CRMs. The framework presented in this study should prove useful in identifying the cause of biases in the moisture–convection relationship in regional and global CRM simulations of the MJO arising from biases in the parameterization of different physics processes.

REFERENCES

Adames, A. F., and D. Kim, 2016: The MJO as a dispersive, convectively coupled moisture wave: Theory and observations. *J. Atmos. Sci.*, **73**, 913–941, doi:10.1175/JAS-D-15-0170.1.

Andersen, J. A., and Z. Kuang, 2012: Moist static energy budget of MJO-like disturbances in the atmosphere of a zonally symmetric aquaplanet. *J. Climate*, **25**, 2782–2804, doi:10.1175/JCLI-D-11-00168.1.

Barnes, H. C., and R. A. Houze, 2013: The precipitating cloud population of the Madden–Julian oscillation over the Indian and west Pacific Oceans. *J. Geophys. Res. Atmos.*, **118**, 6996–7023, doi:10.1002/jgrd.50375.

Bechtold, P., M. Köhler, T. Jung, F. Doblas-Reyes, M. Leutbecher, M. J. Rodwell, F. Vitart, and G. Balsamo, 2008: Advances in simulating atmospheric variability with the ECMWF model: From synoptic to decadal time scales. *Quart. J. Roy. Meteor. Soc.*, **134**, 1337–1351, doi:10.1002/qj.289.

Benedict, J. J., and D. A. Randall, 2007: Observed characteristics of the MJO relative to maximum rainfall. *J. Atmos. Sci.*, **64**, 2332–2354, doi:10.1175/JAS3968.1.

Brown, A. R., 1999: The sensitivity of large-eddy simulations of shallow cumulus convection to resolution and subgrid model. *Quart. J. Roy. Meteor. Soc.*, **125**, 469–482, doi:10.1002/qj.49712555405.

Bryan, G. H., and H. Morrison, 2012: Sensitivity of a simulated squall line to horizontal resolution and parameterization of microphysics. *Mon. Wea. Rev.*, **140**, 202–225, doi:10.1175/MWR-D-11-00046.1.

——, J. C. Wyngaard, and J. M. Fritsch, 2003: Resolution requirements for the simulation of deep moist convection. *Mon. Wea. Rev.*, **131**, 2394–2416, doi:10.1175/1520-0493(2003)131<2394:RRFTSO>2.0.CO;2.

Cheng, A., and K.-M. Xu, 2008: Simulation of boundary-layer cumulus and stratocumulus clouds using a cloud-resolving model with low-and third-order turbulence closures. *J. Meteor. Soc. Japan*, **86A**, 67–86, doi:10.2151/jmsj.86A.67.

——, ——, and B. Stevens, 2010: Effects of resolution on the simulation of boundary-layer clouds and the partition of kinetic energy to subgrid scales. *J. Adv. Model. Earth Syst.*, **2** (3), doi:10.3894/JAMES.2010.2.3.

Chikira, M., 2014: Eastward-propagating intraseasonal oscillation represented by Chikira–Sugiyama cumulus parameterization. Part II: Understanding moisture variation under weak temperature gradient balance. *J. Atmos. Sci.*, **71**, 615–639, doi:10.1175/JAS-D-13-038.1.

Ciesielski, P. E., and Coauthors, 2014: Quality-controlled upper-air sounding dataset for DYNAMO/CINDY/AMIE: Development and corrections. *J. Atmos. Oceanic Technol.*, **31**, 741–764, doi:10.1175/JTECH-D-13-00165.1.

Del Genio, A. D., J. Wu, and Y. Chen, 2012: Characteristics of mesoscale organization in WRF simulations of convection during TWP-ICE. *J. Climate*, **25**, 5666–5688, doi:10.1175/JCLI-D-11-00422.1.

Deng, L., S. A. McFarlane, and J. E. Flaherty, 2013: Characteristics associated with the Madden–Julian oscillation at Manus Island. *J. Climate*, **26**, 3342–3356, doi:10.1175/JCLI-D-12-00312.1.

Deng, M., and Coauthors, 2014: Stratiform and convective precipitation observed by multiple radars during the DYNAMO/AMIE experiment. *J. Appl. Meteor. Climatol.*, **53**, 2503–2523, doi:10.1175/JAMC-D-13-0311.1.

Emanuel, K., A. A. Wing, and E. M. Vincent, 2014: Radiative-convective instability. *J. Adv. Model. Earth Syst.*, **6**, 75–90, doi:10.1002/2013MS000270.

Fridlind, A. M., and Coauthors, 2012: A comparison of TWP-ICE observational data with cloud-resolving model results. *J. Geophys. Res.*, **117**, D05204, doi:10.1029/2011JD016595.

Grabowski, W. W., and M. W. Moncrieff, 2004: Moisture–convection feedback in the tropics. *Quart. J. Roy. Meteor. Soc.*, **130**, 3081–3104, doi:10.1256/qj.03.135.

Hagos, S., 2010: Building blocks of tropical diabatic heating. *J. Atmos. Sci.*, **67**, 2341–2354, doi:10.1175/2010JAS3252.1.

Hannah, W. M., and E. D. Maloney, 2011: The role of moisture–convection feedbacks in simulating the Madden–Julian oscillation. *J. Climate*, **24**, 2754–2770, doi:10.1175/2011JCLI3803.1.

——, and ——, 2014: The moist static energy budget in NCAR CAM5 hindcasts during DYNAMO. *J. Adv. Model. Earth Syst.*, **6**, 420–440, doi:10.1002/2013MS000272.

Hirons, L. C., P. Inness, F. Vitart, and P. Bechtold, 2013a: Understanding advances in the simulation of intraseasonal variability in the ECMWF model. Part I: The representation of the MJO. *Quart. J. Roy. Meteor. Soc.*, **139**, 1417–1426, doi:10.1002/qj.2060.

——, ——, ——, and ——, 2013b: Understanding advances in the simulation of intraseasonal variability in the ECMWF model. Part II: The application of process-based diagnostics. *Quart. J. Roy. Meteor. Soc.*, **139**, 1427–1444, doi:10.1002/qj.2059.

Hohenegger, C., and B. Stevens, 2013: Preconditioning deep convection with cumulus congestus. *J. Atmos. Sci.*, **70**, 448–464, doi:10.1175/JAS-D-12-089.1.

Huffman, G. J., and Coauthors, 2007: The TRMM Multisatellite Precipitation Analysis (TMPA): Quasi-global, multiyear, combined-sensor precipitation estimates at fine scales. *J. Hydrometeor.*, **8**, 38–55, doi:10.1175/JHM560.1.

Iacono, M. J., J. S. Delamere, E. J. Mlawer, M. W. Shephard, S. A. Clough, and W. D. Collins, 2008: Radiative forcing by long-lived greenhouse gases: Calculations with the AER radiative transfer models. *J. Geophys. Res.*, **113**, D13103, doi:10.1029/2008JD009944.

Johnson, D. E., W.-K. Tao, J. Simpson, and C.-H. Sui, 2002: A study of the response of deep tropical clouds to large-scale thermodynamic forcings. Part I: Modeling strategies and simulations of TOGA COARE convective systems. *J. Atmos. Sci.*, **59**, 3492–3518, doi:10.1175/1520-0469(2002)059<3492:ASOTRO>2.0.CO;2.

Johnson, R. H., 1984: Partitioning tropical heat and moisture budgets into cumulus and mesoscale components: Implications for cumulus parameterization. *Mon. Wea. Rev.*, **112**, 1590–1601, doi:10.1175/1520-0493(1984)112<1590:PTHAMB>2.0.CO;2.

——, and P. E. Ciesielski, 2013: Structure and properties of Madden–Julian oscillations deduced from DYNAMO sounding arrays. *J. Atmos. Sci.*, **70**, 3157–3179, doi:10.1175/JAS-D-13-065.1.

——, T. M. Rickenbach, S. A. Rutledge, and P. E. Ciesielski, 1999: Trimodal characteristics of tropical convection. *J. Climate*, **12**, 2397–2418, doi:10.1175/1520-0442(1999)012<2397:TCOTC>2.0.CO;2.

——, P. E. Ciesielski, J. H. Ruppert, and M. Katsumata, 2015: Sounding-based thermodynamic budgets for DYNAMO. *J. Atmos. Sci.*, **72**, 598–622, doi:10.1175/JAS-D-14-0202.1.

Kemball-Cook, S. R., and B. C. Weare, 2001: The onset of convection in the Madden–Julian oscillation. *J. Climate*, **14**, 780–793, doi:10.1175/1520-0442(2001)014<0780:TOOCIT>2.0.CO;2.

Kerns, B. W., and S. S. Chen, 2014: Equatorial dry air intrusion and related synoptic variability in MJO initiation during DYNAMO. *Mon. Wea. Rev.*, **142**, 1326–1343, doi:10.1175/MWR-D-13-00159.1.

Khairoutdinov, M. F., and D. A. Randall, 2003: Cloud resolving modeling of the ARM summer 1997 IOP: Model formulation, results, uncertainties, and sensitivities. *J. Atmos. Sci.*, **60**, 607–625, doi:10.1175/1520-0469(2003)060<0607:CRMOTA>2.0.CO;2.

Kim, D., and Coauthors, 2014: Process-oriented MJO simulation diagnostic: Moisture sensitivity of simulated convection. *J. Climate*, **27**, 5379–5395, doi:10.1175/JCLI-D-13-00497.1.

Kiranmayi, L., and E. D. Maloney, 2011: Intraseasonal moist static energy budget in reanalysis data. *J. Geophys. Res.*, **116**, D21117, doi:10.1029/2011JD016031.

Klingaman, N. P., and Coauthors, 2015: Vertical structure and physical processes of the Madden–Julian oscillation: Linking hindcast fidelity to simulated diabatic heating and moistening. *J. Geophys. Res. Atmos.*, **120**, 4690–4717, doi:10.1002/2014JD022374.

Kodama, Y.-M., M. Katsumata, S. Mori, S. Satoh, Y. Hirose, and H. Ueda, 2009: Climatology of warm rain and associated latent heating derived from TRMM PR observations. *J. Climate*, **22**, 4908–4929, doi:10.1175/2009JCLI2575.1.

Kuang, Z., 2008: Modeling the interaction between cumulus convection and linear gravity waves using a limited-domain cloud system–resolving model. *J. Atmos. Sci.*, **65**, 576–591, doi:10.1175/2007JAS2399.1.

Lang, S., W.-K. Tao, J. Simpson, and B. Ferrier, 2003: Modeling of convective–stratiform precipitation processes: Sensitivity to partitioning methods. *J. Appl. Meteor.*, **42**, 505–527, doi:10.1175/1520-0450(2003)042<0505:MOCSPP>2.0.CO;2.

Ma, D., and Z. Kuang, 2011: Modulation of radiative heating by the Madden–Julian oscillation and convectively coupled Kelvin waves as observed by CloudSat. *Geophys. Res. Lett.*, **38**, L21813, doi:10.1029/2011GL049734.

Madden, R. A., and P. R. Julian, 1971: Detection of a 40–50 day oscillation in the zonal wind in the tropical Pacific. *J. Atmos. Sci.*, **28**, 702–708, doi:10.1175/1520-0469(1971)028<0702:DOADOI>2.0.CO;2.

——, and ——, 1972: Description of global-scale circulation cells in the tropics with a 40–50 day period. *J. Atmos. Sci.*, **29**, 1109–1123, doi:10.1175/1520-0469(1972)029<1109:DOGSCC>2.0.CO;2.

Maloney, E. D., 2009: The moist static energy budget of a composite tropical intraseasonal oscillation in a climate model. *J. Climate*, **22**, 711–729, doi:10.1175/2008JCLI2542.1.

Mapes, B. E., 2004: Sensitivities of cumulus-ensemble rainfall in a cloud-resolving model with parameterized large-scale dynamics. *J. Atmos. Sci.*, **61**, 2308–2317, doi:10.1175/1520-0469(2004)061<2308:SOCRIA>2.0.CO;2.

Masunaga, H., 2013: A satellite study of tropical moist convection and environmental variability: A moisture and thermal budget analysis. *J. Atmos. Sci.*, **70**, 2443–2466, doi:10.1175/JAS-D-12-0273.1.

——, and T. S. L'Ecuyer, 2014: A mechanism of tropical convection inferred from observed variability in the moist static energy budget. *J. Atmos. Sci.*, **71**, 3747–3766, doi:10.1175/JAS-D-14-0015.1.

Matheou, G., D. Chung, L. Nuijens, B. Stevens, and J. Teixeira, 2011: On the fidelity of large-eddy simulation of shallow precipitating cumulus convection. *Mon. Wea. Rev.*, **139**, 2918–2939, doi:10.1175/2011MWR3599.1.

Morrison, H., J. A. Curry, and V. I. Khvorostyanov, 2005: A new double-moment microphysics parameterization for application in cloud and climate models. Part I: Description. *J. Atmos. Sci.*, **62**, 1665–1677, doi:10.1175/JAS3446.1.

——, G. Thompson, and V. Tatarskii, 2009: Impact of cloud microphysics on the development of trailing stratiform precipitation in a simulated squall line: Comparison of one- and two-moment schemes. *Mon. Wea. Rev.*, **137**, 991–1007, doi:10.1175/2008MWR2556.1.

Penide, G., A. Protat, V. V. Kumar, and P. T. May, 2013: Comparison of two convective/stratiform precipitation classification techniques: Radar reflectivity texture versus drop size distribution–based approach. *J. Atmos. Oceanic Technol.*, **30**, 2788–2797, doi:10.1175/JTECH-D-13-00019.1.

Powell, S. W., and R. A. Houze, 2013: The cloud population and onset of the Madden–Julian oscillation over the Indian Ocean during DYNAMO-AMIE. *J. Geophys. Res. Atmos.*, **118**, 11 979–11 995, doi:10.1002/2013JD020421.

Raymond, D. J., 2001: A new model of the Madden–Julian oscillation. *J. Atmos. Sci.*, **58**, 2807–2819, doi:10.1175/1520-0469(2001)058<2807:ANMOTM>2.0.CO;2.

——, and X. Zeng, 2005: Modelling tropical atmospheric convection in the context of the weak temperature gradient approximation. *Quart. J. Roy. Meteor. Soc.*, **131**, 1301–1320, doi:10.1256/qj.03.97.

——, and Ž. Fuchs, 2009: Moisture modes and the Madden–Julian oscillation. *J. Climate*, **22**, 3031–3046, doi:10.1175/2008JCLI2739.1.

Romps, D. M., 2012a: Weak pressure gradient approximation and its analytical solutions. *J. Atmos. Sci.*, **69**, 2835–2845, doi:10.1175/JAS-D-11-0336.1.

——, 2012b: Numerical tests of the weak pressure gradient approximation. *J. Atmos. Sci.*, **69**, 2846–2856, doi:10.1175/JAS-D-11-0337.1.

Rowe, A. K., and R. A. Houze, 2014: Microphysical characteristics of MJO convection over the Indian Ocean during DYNAMO. *J. Geophys. Res. Atmos.*, **119**, 2543–2554, doi:10.1002/2013JD020799.

Schumacher, C., M. H. Zhang, and P. E. Ciesielski, 2007: Heating structures of the TRMM field campaigns. *J. Atmos. Sci.*, **64**, 2593–2610, doi:10.1175/JAS3938.1.

——, S. N. Stevenson, and C. R. Williams, 2015: Vertical motions of the tropical convective cloud spectrum over Darwin, Australia. *Quart. J. Roy. Meteor. Soc.*, **141**, 2277–2288, doi:10.1002/qj.2520.

Smith, P. L., 1984: Equivalent radar reflectivity factors for snow and ice particles. *J. Climate Appl. Meteor.*, **23**, 1258–1260, doi:10.1175/1520-0450(1984)023<1258:ERRFFS>2.0.CO;2.

Sobel, A., and E. Maloney, 2012: An idealized semi-empirical framework for modeling the Madden–Julian oscillation. *J. Atmos. Sci.*, **69**, 1691–1705, doi:10.1175/JAS-D-11-0118.1.

——, and ——, 2013: Moisture modes and the eastward propagation of the MJO. *J. Atmos. Sci.*, **70**, 187–192, doi:10.1175/JAS-D-12-0189.1.

——, J. Nilsson, and L. M. Polvani, 2001: The weak temperature gradient approximation and balanced tropical moisture waves. *J. Atmos. Sci.*, **58**, 3650–3665, doi:10.1175/1520-0469(2001)058<3650:TWTGAA>2.0.CO;2.

——, E. D. Maloney, G. Bellon, and D. M. Frierson, 2010: Surface fluxes and tropical intraseasonal variability: A reassessment. *J. Adv. Model. Earth Syst.*, **2** (2), doi:10.3894/JAMES.2010.2.2.

——, S. Wang, and D. Kim, 2014: Moist static energy budget of the MJO during DYNAMO. *J. Atmos. Sci.*, **71**, 4276–4291, doi:10.1175/JAS-D-14-0052.1.

Steiner, M., R. A. Houze, and S. E. Yuter, 1995: Climatological characterization of three-dimensional storm structure from operational radar and rain gauge data. *J. Appl. Meteor.*, **34**, 1978–2007, doi:10.1175/1520-0450(1995)034<1978:CCOTDS>2.0.CO;2.

Tao, W.-K., C.-L. Shie, J. Simpson, S. Braun, R. H. Johnson, and P. E. Ciesielski, 2003: Convective systems over the South China Sea: Cloud-resolving model simulations. *J. Atmos. Sci.*, **60**, 2929–2956, doi:10.1175/1520-0469(2003)060<2929:CSOTSC>2.0.CO;2.

Thayer-Calder, K., and D. A. Randall, 2009: The role of convective moistening in the Madden–Julian oscillation. *J. Atmos. Sci.*, **66**, 3297–3312, doi:10.1175/2009JAS3081.1.

Tulich, S. N., D. A. Randall, and B. E. Mapes, 2007: Vertical-mode and cloud decomposition of large-scale convectively coupled gravity waves in a two-dimensional cloud-resolving model. *J. Atmos. Sci.*, **64**, 1210–1229, doi:10.1175/JAS3884.1.

Varble, A., and Coauthors, 2011: Evaluation of cloud-resolving model intercomparison simulations using TWP-ICE observations: Precipitation and cloud structure. *J. Geophys. Res.*, **116**, D12206, doi:10.1029/2010JD015180.

——, and Coauthors, 2014: Evaluation of cloud-resolving and limited area model intercomparison simulations using TWP-ICE observations. Part 1: Deep convective updraft properties. *J. Geophys. Res. Atmos.*, **119**, 13 891–13 918, doi:10.1002/2013JD021371.

Wall, C., C. Liu, and E. Zipser, 2013: A climatology of tropical congestus using CloudSat. *J. Geophys. Res. Atmos.*, **118**, 6478–6492, doi:10.1002/jgrd.50455.

Wang, S., and A. H. Sobel, 2011: Response of convection to relative sea surface temperature: Cloud-resolving simulations in two and three dimensions. *J. Geophys. Res.*, **116**, D11119, doi:10.1029/2010JD015347.

——, and ——, 2012: Impact of imposed drying on deep convection in a cloud-resolving model. *J. Geophys. Res.*, **117**, D02112, doi:10.1029/2011JD016847.

——, ——, and Z. Kuang, 2013: Cloud-resolving simulation of TOGA-COARE using parameterized large-scale dynamics. *J. Geophys. Res. Atmos.*, **118**, 6290–6301, doi:10.1002/jgrd.50510.

——, ——, F. Zhang, Y. Q. Sun, Y. Yue, and L. Zhou, 2015: Regional simulation of the October and November MJO events observed during the CINDY/DYNAMO field campaign at gray zone resolution. *J. Climate*, **28**, 2097–2119, doi:10.1175/JCLI-D-14-00294.1.

Xu, K.-M., 1995: Partitioning mass, heat, and moisture budgets of explicitly simulated cumulus ensembles into convective and stratiform components. *J. Atmos. Sci.*, **52**, 551–573, doi:10.1175/1520-0469(1995)052<0551:PMHAMB>2.0.CO;2.

——, and D. A. Randall, 1996: Explicit simulation of cumulus ensembles with the GATE Phase III data: Comparison with observations. *J. Atmos. Sci.*, **53**, 3710–3736, doi:10.1175/1520-0469(1996)053<3710:ESOCEW>2.0.CO;2.

Xu, W., and S. A. Rutledge, 2014: Convective characteristics of the Madden–Julian oscillation over the central Indian Ocean observed by shipborne radar during DYNAMO. *J. Atmos. Sci.*, **71**, 2859–2877, doi:10.1175/JAS-D-13-0372.1.

Yanai, M., S. Esbensen, and J.-H. Chu, 1973: Determination of bulk properties of tropical cloud clusters from large-scale heat and moisture budgets. *J. Atmos. Sci.*, **30**, 611–627, doi:10.1175/1520-0469(1973)030<0611:DOBPOT>2.0.CO;2.

Yang, S., and E. A. Smith, 2000: Vertical structure and transient behavior of convective–stratiform heating in TOGA COARE from combined satellite–sounding analysis. *J. Appl. Meteor.*, **39**, 1491–1513, doi:10.1175/1520-0450(2000)039<1491:VSATBO>2.0.CO;2.

Yoneyama, K., C. Zhang, and C. N. Long, 2013: Tracking pulses of the Madden–Julian oscillation. *Bull. Amer. Meteor. Soc.*, **94**, 1871–1891, doi:10.1175/BAMS-D-12-00157.1.

Yu, L., and R. A. Weller, 2007: Objectively analyzed air–sea heat fluxes for the global ice-free oceans (1981–2005). *Bull. Amer. Meteor. Soc.*, **88**, 527–539, doi:10.1175/BAMS-88-4-527.

Yuter, S. E., and R. A. Houze, 1997: Measurements of raindrop size distributions over the Pacific warm pool and implications for *Z–R* relations. *J. Appl. Meteor.*, **36**, 847–867, doi:10.1175/1520-0450(1997)036<0847:MORSDO>2.0.CO;2.

Zhang, C., 2005: Madden–Julian oscillation. *Rev. Geophys.*, **43**, RG2003, doi:10.1029/2004RG000158.

——, 2013: Madden–Julian Oscillation: Bridging weather and climate. *Bull. Amer. Meteor. Soc.*, **94**, 1849–1870, doi:10.1175/BAMS-D-12-00026.1.

Zuluaga, M. D., and R. A. Houze, 2013: Evolution of the population of precipitating convective systems over the equatorial Indian Ocean in active phases of the Madden–Julian oscillation. *J. Atmos. Sci.*, **70**, 2713–2725, doi:10.1175/JAS-D-12-0311.1.